PHYSICAL REVIEW C VOLUME 51, NUMBER 4 APRIL 1995

Entrance-channel dependence of the fission dynamics in ^{19}F+^{209}Bi vs ^{64}Ni+^{165}Ho

K. Knoche, L. Lüdemann, and W. Scobel
I. Institut für Experimentalphysik, Universität Hamburg, Germany

B. Gebauer, D. Hilscher, D. Polster, and H. Rossner
Hahn-Meitner-Institut, Berlin, Germany

(Received 7 October 1994)

Binary fragmentations of ^{19}F + ^{209}Bi (E_p = 491 MeV) and ^{64}Ni + ^{165}Ho (E_p = 778 MeV) leading to compound nuclei with $E^* \approx 400$ MeV and similar masses were investigated by measuring fission coincident neutrons and α particles. The neutron field was decomposed into contributions from preequilibrium (PE), prescission, and the two fragment sources with a moving source analysis. It was performed for separate excitation energy classes deduced with the folding angle technique from the linear momentum transfer. The angular distribution of the PE neutrons from the ^{19}F + ^{209}Bi reaction indicates a pronounced out-of-plane anisotropy that would result in an overestimation of the PE multiplicity by 37% for a measurement only in plane. The PE multiplicities and temperatures are interpreted by a delay in formation for the more symmetric entrance channel ^{64}Ni + ^{165}Ho, which is typical for quasifission and in line with the enhancement of asymmetric mass splits. Prescission times derived from the neutron clock method extend from 30×10^{-22} s for ^{64}Ni + ^{165}Ho to 160×10^{-22} s for ^{19}F + ^{209}Bi. Here, a constant level density parameter of $A/10\,\mathrm{MeV}^{-1}$ was used which is an outcome of the simultaneous measurement of α emission temperatures. The prescission times are qualitatively discussed in terms of the reaction dynamics.

PACS number(s): 25.70.Jj, 24.60.−k

I. INTRODUCTION

The mechanism of heavy ion induced binary fission gives valuable insights into the process of distortion of nuclear matter [1]. It is now well established that the fission process is distinctly slower than particle evaporation for excitation energies above approximately 50 MeV, because nuclear matter must be rearranged during fission. This delay becomes experimentally accessible by the enhancement of neutron [3,4], charged particle [2] emission, or γ decay modes [5] prior to scission. Prescission times deduced with these methods seem to be approximately independent of initial excitation energies [3,6,7] and fissility [4,1].

Conventionally, one has to distinguish between three different time intervals contributing to the dynamical time scale, namely the equilibration time τ_{PE} for compound nucleus (CN) thermalization, the transit time τ_t to reach a constant probability flow across the saddle point, and the saddle-to-scission time τ_{ss} to develop from the saddle point to the scission point configuration.

Calculations with a Boltzmann master equation (BME) approach [8], together with preequilibrium neutron multiplicities, reveal equilibration times τ_{PE} on the order of 5×10^{-22} s.

The experimental separation of prescission and postscission neutrons based on their different kinematical focusing, i.e., the neutron clock method, provides only the sum $\tau_t + \tau_{\mathrm{ss}}$ of the transit and saddle-to-scission times. For heavy systems of mass $A \approx 200$ u, typical prescission times $\tau_{\mathrm{pre}} = \tau_t + \tau_{\mathrm{ss}}$ between 5×10^{-21} s and 3×10^{-20} s are anticipated [9]. However, it is an unsolved problem whether τ_t or τ_{ss} dominates the prescission time. A simultaneous measurement of prescission neutrons and charged particles indicates a dominating saddle-to-scission time [10,11]. It has also been argued that fission excitation probabilities are indicative for the bulk of the prescission emissions to occur prior to the saddle point [12]; this argumentation, however, is inconclusive [13].

Concerning the entrance channel impact [14,15], it has been suggested that the formation process during heavy ion collisions is hindered for more mass symmetric entrance channels. Whereas statistical model calculations can describe γ spectra from the ^{16}O + ^{148}Sm reactions, they fail to reproduce the γ spectra for the more symmetric entrance channel ^{64}Ni + ^{100}Mo [16], and the total neutron multiplicity observed for the system ^{64}Ni + ^{92}Zr was smaller than predicted by the statistical model [17]. It has also been shown that the mass splits of the reaction products from ^{40}Ar + ^{232}Th are preferentially asymmetric, whereas the mass split distribution of ^{32}S + ^{238}U is symmetric [18]. Together, these observations indicate a longer formation time for more symmetric entrance channels. However, for the reactions quoted in this paragraph, the formation times overlap with those corresponding to evaporation from an equilibrated compound nucleus.

To further pursue the influence of the entrance channel on reaction systems, reactions have been chosen which lead to comparable masses $A \geq 200$ and excitation energies $E^* \geq 200$ MeV of the compound nuclei. Comparison of the data is expected to yield information on the influence of the formation mechanism and of the fission barrier on the temporal evolution of heavy ion induced fission. Furthermore, it can be expected that formation times overlap with the preequilibrium phase because of

0556-2813/95/51(4)/1908(18)/$06.00

the higher projectile velocities.

In order to investigate the prescission time accurately by means of the neutron clock, it is necessary to determine the energy balance of the whole deexcitation cascade and in particular to fix the level density parameter a, which is not well known for the excitation energies under discussion. Holub *et al.* [19] and Hilscher *et al.* [20] have deduced a level density parameter $a = A/(10.5 \pm 1)\,\mathrm{MeV}^{-1}$ for CN with mass numbers $A \approx 180$ by comparing the slope of neutron energy spectra with statistical model calculations. This result was confirmed by Chbihi *et al.* [21] from a comparison between proton and deuteron spectra for $A \approx 110$ and excitation energies between 1.3 and 3.0 MeV/nucleon. On the other hand, Nebbia *et al.* [22] deduced level density parameters for neutrons and charged particles, which increase from $A/13$ to $A/10\,\mathrm{MeV}^{-1}$ for initial excitation energies between 2 to 4.3 MeV/nucleon. Hence, in this work the determination of the level density parameter is performed by exploiting both α and neutron emission spectra.

The paper is organized as follows: Sec. II explains the experimental procedure and Sec. III describes the data reduction for the fragments, the coincident neutrons, and α particles. In Sec. IV the results for the preequilibrium (PE) source parameters are discussed. Sec.V is devoted to an interpretation of the prescission and postscission source parameters. In Sec. VI the prescission neutron multiplicities together with a statistical model calculation are interpreted in terms of prescission time scales. Section VII summarizes our work.

II. EXPERIMENTAL PROCEDURE

The experiment was performed with ^{64}Ni and ^{19}F projectiles with energies of 778 MeV (12.2 MeV/nucleon) and 491 MeV (26.1 MeV/nucleon), respectively, from the VICKSI accelerator at the Hahn-Meitner Institut Berlin. The self-supporting, monoisotopic metallic targets of $500\,\mu\mathrm{g/cm}^2$ thickness were mounted inside a thin walled scattering chamber. The accelerator was operated with burst repetitions of 17.1 MHz (18.5 MHz), widths $\Delta t \approx$ 1.2 ns (0.9 ns) (FWHM) for the ^{64}Ni (^{19}F) beam and time-averaged beam currents of typically 0.33 particle nA (0.74 particle nA) that corresponded to luminosities L of $3.4 \times 10^{27}\,\mathrm{cm}^{-2}\,\mathrm{s}^{-1}$ ($11.4 \times 10^{27}\,\mathrm{cm}^{-2}\,\mathrm{s}^{-1}$). These numbers, as well as the beam position monitoring, were deduced from the elastically scattered projectiles observed in two small plastic scintillators at $\Theta_{\mathrm{lab}} = \pm 10.5°$ in the reaction plane.

The detector setup inside and around the scattering chamber is shown schematically in Fig. 1(a) for the ^{64}Ni + ^{165}Ho experiment we shall describe first. It consists of low-pressure multiwire chambers (MWC) of active sizes 61 mm×61 mm and 122 mm× 244 mm on both sides of the beam, supplemented by a fourfold segmented surface barrier detector array (SB) of $315\,\mu$m thickness and 26 cm^2 active area. Further data are listed in Table I. The angular acceptance $\Delta\Psi$ out of plane extended to $\pm 13°$. The MWC's provided two-dimensional position ($\Delta x, y \approx 0.8$ mm FWHM) and timing ($\Delta t \approx 240$ ps FWHM) information , which was used for the reconstruction of kinematic coincidences between fragmentlike reaction products. The MWC's were centered around the angles $\Theta_{\mathrm{MWC}} = \pm 42°$, which correspond to the most probable linear momentum transfer (LMT) of 95% for symmetric fragmentation [23]. Their detection efficiencies extend to 20% and beyond 100% LMT, respectively.

Time and pulse height measurements made with the surface barrier detectors in coincidence with the large MWC allowed an independent determination of binary fission events. The pulse height calibration was performed with a ^{252}Cf source brought in target position; pulse height defects were accounted for [24,25] as well as the energy loss of charged particles in the target [7,9]. Charged particle velocities were determined with an absolute time scale derived from symmetric fragmentations for which the total kinetic energy (TKE) was known from the pulse height measured with the SB's 1,2 [7,9,26]. The overall time resolution received contributions from the burst width and the detector resolution, including, for

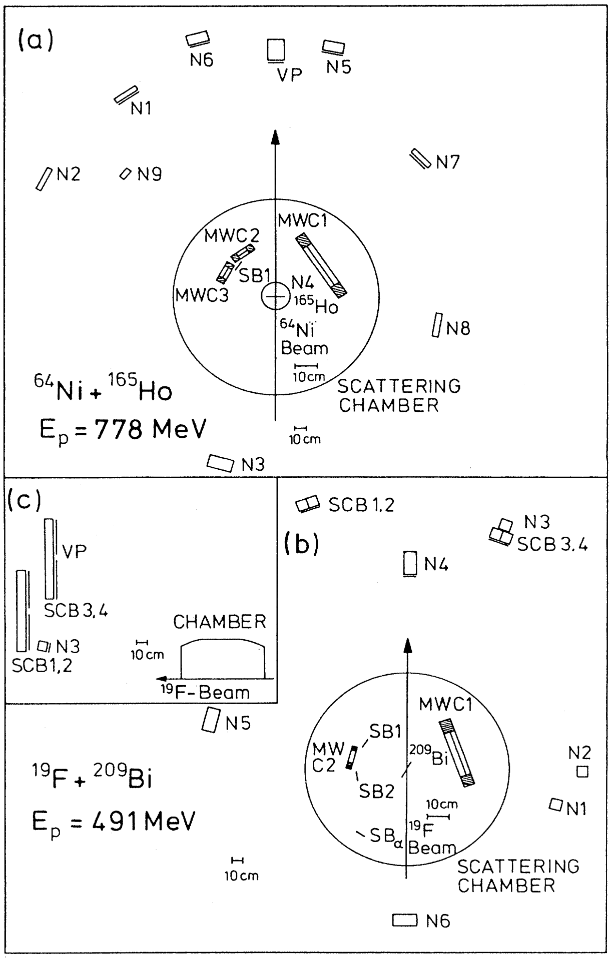

FIG. 1. Experimental setup consisting of neutron detectors N_i (some with veto paddles VP), position sensitive multiwire chambers MWC$_i$ and surface barrier detectors SB$_i$ for (a) the reaction ^{64}Ni + ^{165}Ho and (b) the reaction ^{19}F + ^{209}Bi. Inset (c) shows the setup of the position sensitive scintillator bars SCB$_i$ from a side view.

TABLE I. Geometry of fragment detectors.

Reaction	Detector	TOF path (mm)	Φ (deg)	Ψ (deg)
$^{64}Ni + ^{165}Ho$	MWC1	272	-31.5 / -78.9	-12.6 / 12.6
	MWC2	270	30.0 / 41.7	-6.4 / 6.4
	MWC3	270	57.1 / 68.8	-6.4 / 6.4
	SB1	236	42.9 / 55.3	-6.6 / 6.4
$^{19}F + ^{209}Bi$	MWC1	264	-44.7 / 93.3	-13.1 / 13.1
	MWC2	276	70.6 / 83.3	-6.4 / 6.4
	SB1	257	51.8 / 63.3	-5.7 / 5.7
	SB2	255	92.0 / 104.1	-6.1 / 6.1
	SB_α	407	143.5 / 150.8	-3.6 / 3.6

the SB's 1,2, the uncertainties in the plasma delay correction [27].

For neutron time-of-flight (TOF) spectroscopy we used ten cylindrical cells, typically of 25 cm diameter and 10 cm thickness, filled with liquid scintillator materials NE213 or BC501. They had n-γ pulse shape discrimination capabilities and were arranged around the reaction chamber within as well as outside of the reaction plane, with distances varying from 1.0 m to 2.3 m and reaction angles $\Theta_{\mathrm{lab},n}$ between 0° and 163°. The scintillator cells were equipped in front with 3 mm lead to suppress excessive γ radiation. Most of them (see Fig. 1) also had a scintillator veto paddle in front for discrimination against energetic charged reaction particles. The neutron detection efficiencies $\eta(E_n^{\mathrm{thr}},E_n)$ were calculated for $E_n \leq 20\,\mathrm{MeV}$ with the code NEFF4 [28]; for higher neutron energies they were obtained with the CECIL code [29]. The thresholds E_n^{thr} were on the order of 1 MeV equivalent neutron energy; they were derived from the 90% points of the Compton edges observed for several γ sources. For each individual neutron detector we obtained the overall time resolution from the prompt target γ peak of up to 2 ± 0.4 ns for the full dynamic range above threshold.

The neutron flux attenuation due to construction material in the TOF paths was accounted for with the code ATTENE [30]. The estimated uncertainties of the efficiency determination ($\leq 8\%$), the absorption correction ($< 10\%$), and the background subtraction ($< 10\%$) yielded an overall uncertainty of less than 15%. Uncertainties in the resulting total neutron multiplicities M_{tot} tend to be smaller; this is the outcome of an independent and supplementary experiment performed with a 4π scintillator tank for the reaction $^{32}S + ^{197}Au$ at 26.2 MeV/nucleon [31]. The uncertainties in partial neutron multiplicities resulting from moving source fits to the fission coincident neutron TOF data are quoted in Sec. III B.

Data collection was triggered by a coincidence of two fission fragments on either side of the beam direction; it also allowed us to identify unambiguously the correct cyclotron RF signal needed for all TOF measurements.

The $^{19}F + ^{209}Bi$ experiment was performed with detector elements of the type used for the $^{64}Ni + ^{165}Ho$ study, but in a geometry schematically shown in Fig. 1(b) and with the geometrical data listed in Table I. Comparison of Fig. 1(b) with Fig. 1(a) exhibits differences that fall essentially into three categories:

(i) Due to the smaller linear momentum transferred with ^{19}F and the accordingly lower velocity of the center of mass, the folding angle for the anticipated [23] most probable LMT of about 78% is larger than in the $^{64}Ni + ^{165}Ho$ study. The fragment detectors were therefore centered around $\Theta_{\mathrm{MWC}} = \pm 68°$. The target was tilted to minimize the energy loss of the fragments; the effective target thickness corresponded to an average energy loss of 3.4 MeV per fragment for symmetric fragmentations.

(ii) In order to facilitate the spectroscopy of fragment energies, one of the two MWC's on the left arm was replaced by a fourfold segmented surface barrier detector (SB2); a third, twofold one (SB_α) was placed at a backward angle so that it would be particularly sensitive to α particles from equilibrium processes.

(iii) Most important, four plastic scintillator bars SCB1–SCB4 of size 10 cm×10 cm×100 cm made from BC408 were added for neutron detection in the forward hemisphere. Details of their performance are discussed in [32]. They were read out on both sides for position-sensitive neutron TOF spectroscopy by the time difference technique. The position resolution was $\Delta x \leq 5\,\mathrm{cm}$ (FWHM) along the axis for deposited energies a factor two and more above typical threshold values $E_n^{\mathrm{thr}} \approx 4\,\mathrm{MeV}$. With such thresholds, γ background could effectively be suppressed. Since they were installed perpendicular to the reaction plane [see Fig. 1(c)] the scintillator bars covered out-of-plane angles Ψ up to 45°, and thus allowed us to measure relative neutron angular distributions in this direction with a minimum of systematic errors. The SCB neutron detection efficiencies as a function of E_n were determined with the CECIL code [29]; absolute values were derived from a comparison of detector N3 and its well-known efficiency to the homologous segment of SCB2. Additional efficiency checks were performed with the fission coincident neutrons from a ^{252}Cf source [32]. For experimental reasons [32], the usable detector length was restricted to $5\,\mathrm{cm} \leq x \leq 95\,\mathrm{cm}$. The detector data were analyzed for nine bins of 10 cm, which were grouped in some cases to segments of 30 cm length to improve the statistics.

III. DATA REDUCTION AND EXPERIMENTAL RESULTS

A. Fission fragments

The general reaction model used as a starting point for the analysis is that of a binary fragmentation following an incomplete fusion with a linear momentum transfer LMT whose determination is based on the spectator model.

The composite system CN which later undergoes fission has a recoil velocity $v_\parallel$ in projectile direction that is calculated from the observed fragment velocities (v_1, v_2), the laboratory angles Φ_1, Φ_2 relative to the beam direction (i.e., $\cos\Phi_i = \cos\Theta_i \cos\Psi_i$), and their folding angle $(\Phi_1 + \Phi_2)$:

$$v_\parallel = \frac{v_1 v_2 \sin(\Phi_1 + \Phi_2)}{v_1 \sin\Phi_1 + v_2 \sin\Phi_2} \,. \tag{1}$$

If $m'_{\rm CN}$ is the mass of the system remaining after particle evaporation, then the fragment masses $m_1, m_2 = m'_{\rm CN} - m_1$ are given by

$$m_1 = m'_{\rm CN} \frac{v_2 \sin\Phi_2}{v_1 \sin\Phi_1 + v_2 \sin\Phi_2} \,. \tag{2}$$

The ratio $m_1/m'_{\rm CN}$ will be referred to as the normalized mass M_N. In the massive transfer model, the spectator part of the projectile proceeds in the projectile direction with a velocity v_p, such that the linear momentum transferred is

$$\text{LMT} = \frac{v_\parallel}{v_0} \frac{1}{1 + \frac{m_P}{m_T}(1 - \frac{v_\parallel}{v_0})} \,, \tag{3}$$

where v_0 equals $v_\parallel$ for complete fusion and m_p is the projectile mass.

Application of Eq. (2) requires $m'_{\rm CN}$ as input; it is calculated as

$$m'_{\rm CN} = m_T + \text{LMT} \times m_p - m_{\rm evap} \,, \tag{4}$$

where the correction $m_{\rm evap}$ for particle evaporation from the composite system and the fragments is calculated with a statistical model starting at the excitation energy $E^*_{\rm CN}(\text{LMT})$ remaining after equilibration [9]:

$$E^*_{\rm CN}(\text{LMT}) = E_p \times \text{LMT} \frac{m_T}{m_T + \text{LMT} \times m_p} \times \sqrt{1 - \left(\frac{v_p}{c}\right)^2} + Q(\text{LMT}) \,. \tag{5}$$

Here, the first term denotes the part of the kinetic energy E_p of the projectile in the laboratory frame that is transferred and dissipated. Based on the arguments given in [9], no correction for preequilibrium particle emission is included in Eq. (5) beyond the amount carried away by the spectator part. The ground state values $Q(\text{LMT})$ for incomplete fusion were calculated from mass tables [33].

For further analysis the events were subdivided into classes corresponding to symmetric ($0.4 \le M_N \le 0.6$) and asymmetric fragmentations, and into the intervals ΔLMT listed in Table II. The assumed projectile fragmentations given there include a correction for the experimentally observed PE neutron multiplicity $\mathrm{M_{PE}}(\text{LMT})$, cf. Sec. IV.

A total of about 5×10^7 binary fragmentations were analyzed in the framework of this model. The resulting LMT distributions in Figs. 2(c) and 2(d) show clearly distinctive patterns. The majority of the ^{64}Ni + ^{165}Ho events occurs with an almost complete LMT, i.e., as a central collision. These events are well separated from a small group of peripheral collisions at LMT $\approx$30%, which are cut off by the finite solid angle coverage of the detector system. The most probable LMT of 98% is in good agreement with recent compilations of this quantity as a function of the entrance channel energy above the Coulomb barrier [23]. The two-dimensional contour diagram of the LMT vs M_N plane [Fig. 2(f)] shows that in the central collisions, despite the high excitation energy $E^*_{\rm CN} > 300$ MeV (cf. Table II), the asymmetric fragmentations prevail. They occur with total kinetic energies (TKE) far above the values anticipated for systems developing towards scission after *total* dissipation of the kinetic energy in the entrance channel. This is visible in Fig. 2(b), where the asymmetric fragmentations carry TKE up to twice as high as observed for fusion-fission events. Both fragmentation as well as TKE therefore indicate a fast, deep inelastic reaction mechanism like in quasifission, where the composite system breaks apart before mass equilibration is completed. In contrast, the

TABLE II. LMT windows with centroids ⟨LMT⟩ applied in the analysis of the reactions ^{64}Ni+^{165}Ho, ^{19}F+^{209}Bi. They are referred to as 1(a)–2(d). For each window are given the fragmentation into PE nucleons, spectator, and CN following participant absorption, and $E^*_{\rm CN}$ resulting from Eq. (5).

Reaction	LMT window		⟨LMT⟩	$E^*_{\rm CN}$ (MeV)	Fragmentation
^{64}Ni + ^{165}Ho	1(a)	20% – 65%	47%	220	^{197}Hg + ^{24}Mg + $3p + 5n$
	1(b)	66% – 89%	80%	320	^{216}Ac + ^{8}Be + $2p + 3n$
	1(c)	90% – 100%	96%	360	^{227}Pu + $1p + 1n$
	1(d)	101% – 110%	100%	370	^{229}Am
^{19}F + ^{209}Bi	2(a)	20% – 50%	35%	130	^{216}Fr + ^{8}Be + $1p + 3n$
	2(b)	51% – 69%	60%	240	^{220}Ac + ^{4}He + $1p + 3n$
	2(c)	70% – 90%	80%	300	^{224}Pa + $1p + 3n$
	2(d)	91% – 110%	100%	390	^{228}U

symmetric fragmentations $M_N \approx 0.5$ correlate with TKE in complete agreement with the fusion-fission systematics, in particular if the mass depletion by particle evaporation prior to scission is taken care of with a statistical model calculation, details of which are given in Sec.V.

The fusion of ^{19}F with ^{209}Bi follows a different pattern, one that is much more like $^{32}\text{S} + {}^{197}\text{Au}$ at the same projectile energy per nucleon [9]. The most probable LMT is 78% and the preferred fission mode is the symmetric one [Figs. 2(a) and 2(e)]. The TKE values for the mass symmetric and most of the asymmetric fission events are in line with the systematics for equilibrated systems; deep inelastic contributions are visible, too, but do not prevail.

The LMT distribution found for $^{19}\text{F} + {}^{209}\text{Bi}$ in Fig. 2(c) is obviously broader and less pronounced than that for $^{64}\text{Ni} + {}^{165}\text{Ho}$. This is not necessarily a feature of the reaction mechanism, but may rather be an artifact of the mode of analysis. The determination of the LMT with Eq. (3) hinges on the velocity component $v_{\|}$. It is derived from the fragment velocities v_1, v_2 *after* particle emission [Eq. (1)]. These velocities are therefore not necessarily coplanar any more, and even the compound nucleus at scission has experienced recoils from particle evaporation and incomplete linear momentum transfer. A measure for such distortions perpendicular to the reaction plane is the out-of-plane angle $\Delta\Psi = \Psi_2 - \Psi_1$ of the two fragments [31]. Analysis of the MWC position informations reveals Gaussian distributions for $\Delta\Psi$ centered in the reaction plane. Their widths $\delta(\Delta\Psi)$ are about 12° (FWHM) for the central collision peaks of both reactions. Assuming in-plane the same distortions, we get variations of the LMT that are considerably smaller for Ni+Ho (22%) than for F+Bi (39%), because the ^{64}Ni projectiles with 9630 MeV/c carry a much higher absolute linear momentum into the reaction than the ^{19}F projectiles (4170 MeV/c) do. The former's LMT distributions therefore tend to be less smeared out.

It should be mentioned that the populations presented in Figs. 2(e) and 2(f) are corrected for the detector efficiency. For this purpose, a Monte Carlo simulation of binary fragmentations with a $(\sin\Theta_{\text{cms}})^{-1}$ angular distribution was performed for the actual detector geometry. The calculation of the total kinetic energy (TKE) of both fragments was based on the systematics given in [34], with corrections for the mass asymmetry [35] and for prescission particle emission to the extent indicated [9] by the LMT value. With this input, the fraction of detected fission events can be calculated for each bin in the LMT vs M_N plane and applied to experimental data parametrized in this way.

The fusion-fission cross section σ_{fiss} for both reactions can be estimated from limiting angular momenta. The fusion potentials based on the Bass nuclear potential [36] are shown in Fig. 3 for $l = 0$ and l^B_{crit}, where the latter denotes the partial wave with vanishing potential pocket. Their values $l^B_{\text{crit}} = 120\hbar$ $(82\hbar)$ for $^{64}\text{Ni} + {}^{165}\text{Ho}$ $({}^{19}\text{F} + {}^{209}\text{Bi})$ represent an upper limit for fusion-fission,

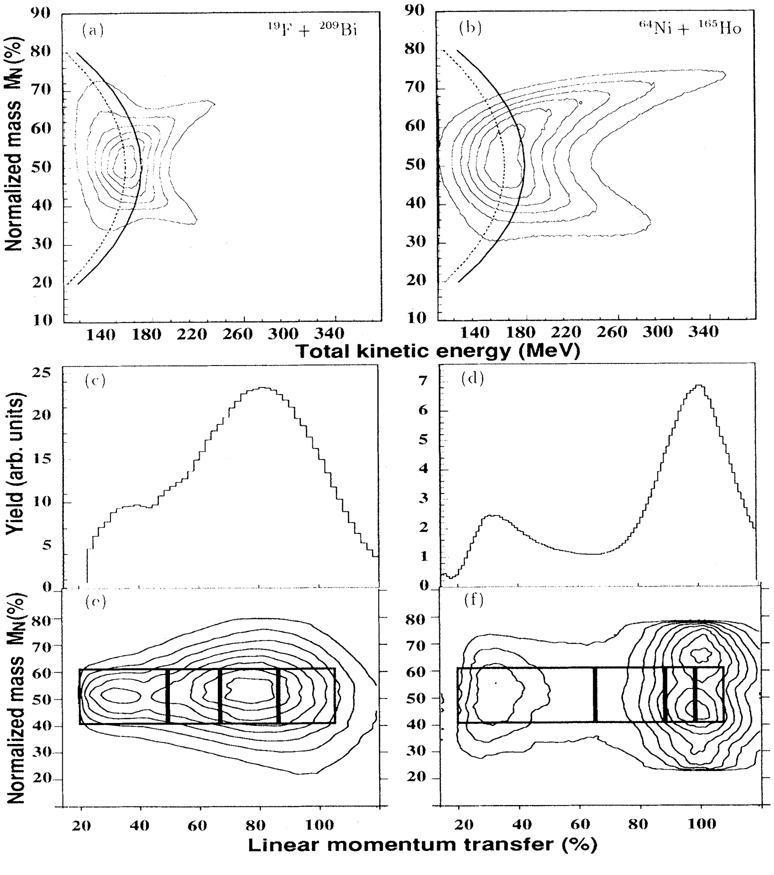

FIG. 2. (a), (b) Contour plot of total kinetic energy TKE vs normalized mass M_N; the yield increases by 14% between adjacent lines. Also shown is the expected TKE from Viola's systematics [34] extended to asymmetric mass splits [35], both without (solid line) and with (dotted) particle emission prior to scission. (c), (d) LMT distribution after correction for the detector efficiency. (e), (f) Contour plot of the LMT vs M_N after correction for the detector efficiency; the yield increases by 11% between adjacent lines. The boxes separate the fragmentation classes applied for data analysis.

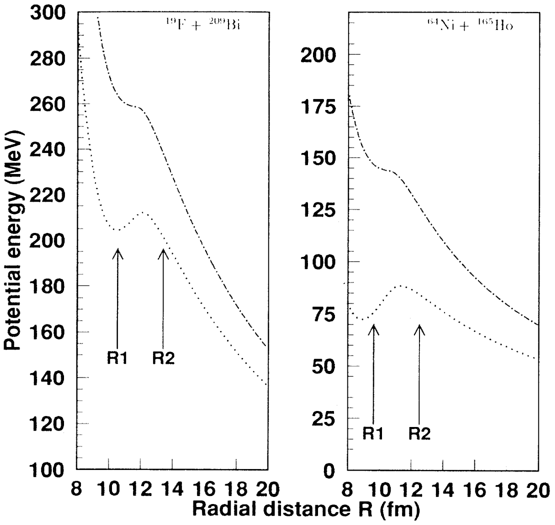

FIG. 3. Fusion potentials from Bass [36] as a function of the distances between projectile and target for $l = 0$ (dotted) and $l = l^B_{\rm crit}$ (dash-dotted). The arrows point to the equilibrium shape (R1) and interaction (R2) radius, respectively.

because the compound nuclei resulting after the most probable linear momentum transfer are of high fissility x= 0.81 (0.78). Their fission barriers as calculated in the rotating liquid drop model [37] vanish for $l_0 = 67\hbar$ ($74\hbar$). Therefore, even if fusion with $l \leq l_0$ is assumed to always lead to subsequent fission, the associated compound nucleus fission cross section $\sigma_{\rm fiss}$ represents only a fraction of the total fusion cross section $\sigma_{\rm fus} = (\lambda^2/4\pi)(l^B_{\rm crit}+1)^2$, namely 0.32 (0.82).

For comparison, the experimental cross sections for fusion were derived by putting together the luminosities L obtained from the elastic scattering monitors and the number of binary fission events $N_{\rm cc}$ occurring in the central collision (cc) peaks around the most probable LMT [cf. Figs. 2(c) and (d)] with corrections for detection efficiency and extrapolation into the full 2π solid angle coverage in the center-of-mass system. Conversion of $\sigma_{\rm cc}$ into the corresponding $l_{\rm cc}$ yields $134\hbar$ ($123\hbar$) for ^{64}Ni + ^{165}Ho (^{19}F + ^{209}Bi). These are, however, not the angular momenta found in the fused systems, because angular momentum is carried away in the preequilibrium reaction phase to an extent reflected in the *linear* momentum not transferred. The corresponding loss of angular momentum Δl can be derived from the simple approximation [8], $\Delta l(\hbar) \approx 0.34(1-{\rm LMT}_{\rm mp})\sqrt{A_pE_p}A^{1/3}_{\rm CN}$. Here, ${\rm LMT}_{\rm mp}$ is the most probable LMT for central collisions, $\sqrt{A_pE_p}$ is proportional to the absolute projectile momentum, and $A^{1/3}_{\rm CN}$ is a measure of the radius of the CN formed. One finds a reduction of $l_{\rm cc}$ by $\Delta l = 9\hbar$ ($40\hbar$) for ^{64}Ni + ^{165}Ho (^{19}F + ^{209}Bi), leading to $l_{\rm crit} = l_{\rm cc} - \Delta l = 125\hbar$ ($83\hbar$). These values are in good agreement with those obtained for $l^B_{\rm crit}$ and show the same excess over the fission barrier limits l_0.

Central collisions in ^{64}Ni + ^{165}Ho are therefore expected to proceed primarily through exit channels with no fission barrier, i.e., as fast fission [38,39] without total dissipation of the initial kinetic energy into intrinsic excitation; for ^{19}F + ^{209}Bi , the sequential fusion-fission mode dominates.

B. Fission coincident neutrons

The analysis of the measured double differential neutron multiplicities $M_n(E_n, \Theta_n)$ was performed for the different LMT and M_N classes, respectively. For each fragmentation class the multiplicities were decomposed into the contributions of four moving sources, namely a preequilibrium (PE) source, a compound nucleus (CN) source, and two sources of fully accelerated fragments (F1,F2). Each source is assumed to emit its neutrons isotropically in its own rest frame with a spectral shape of a Watt distribution. After transformation into the laboratory frame and normalization, one obtains for the total double differential neutron multiplicities

$$\frac{d^2M_{\rm tot}(E_n,\Theta_n)}{dE_n\,d\Omega(\Theta_n)} = \sum_{i=1}^{4}\frac{M_{n,i}}{2(\pi T_{n,i})^{3/2}}\sqrt{E_n} \times \exp\left[-\frac{E_n+\epsilon_i-2\sqrt{E_n\epsilon_i}\cos\Theta_i}{T_{n,i}}\right]. \qquad (6)$$

Here $M_{n,i}$ is the neutron multiplicity and ϵ_i the source velocity of the ith source. The temperature parameters T_i are the averages over the whole deexcitation cascade and are related to the initial temperature of each source by $T_{0,i} = 12/11 \cdot T_i$. The emission angle Θ_i was measured with respect to the momentum direction of each source. The free fit parameters were the multiplicities M_i and temperatures T_i for the four sources, and the source velocity of the PE source. The source velocities of the CN and the fragment sources were averaged over the fragment events under consideration. Here, special attention was given to the spectra of the liquid scintillators that are most sensitive to the fragment source F1, i.e., N7 and N8 for ^{64}Ni + ^{165}Ho, and N1 and N2 for ^{19}F + ^{209}Bi. For F2 these are N1, N2, and N9 for ^{64}Ni + ^{165}Ho, and N5 for ^{19}F + ^{209}Bi. The spectra of the former reaction were divided into four subgroups, depending on the segment of MWC1 in which the coincident fragment was detected and those of the latter one into three subgroups corresponding to the three fragment detectors.

In a first step, the right-hand side of Eq. (6) was evaluated by performing a least squares fit that included all liquid scintillators simultaneously. In the next step the resulting parameter sets were used to deduce the multiplicity and temperature of the CN source from a fit to the spectra of the most backward liquid scintillators, because these spectra are least sensitive to contributions from sources other than the CN. In a third step the resulting CN temperature parameter was fixed and the remaining parameters released for all scintillators. Steps 2 and 3 were repeated until convergence was reached after 2 or 3 iterations. The individual uncertainty of one parameter was estimated by changing it until χ^2 increased by 10% over its minimum value.

Figures 4 and 5 show the α spectra to be discussed in

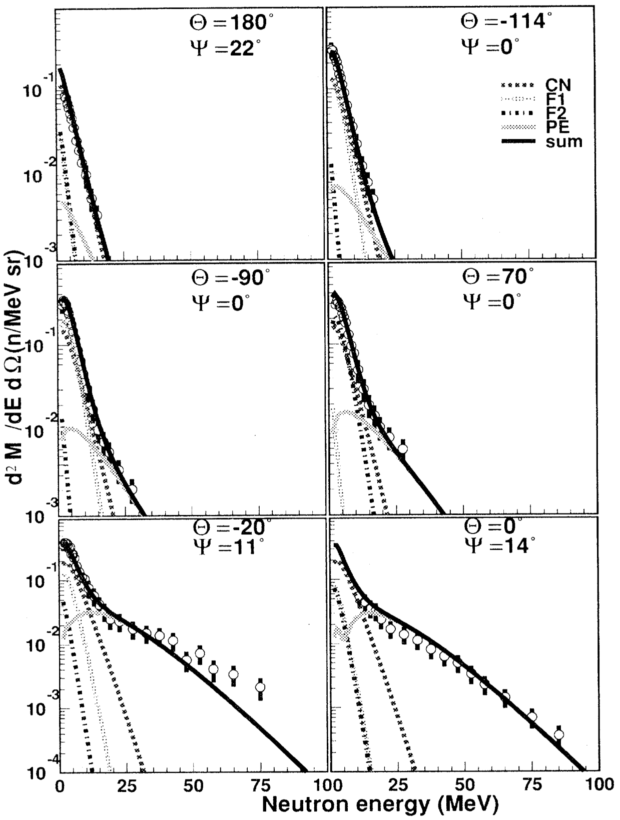

FIG. 4. Representative double differential neutron multiplicities (open circles) measured with liquid scintillators for symmetric fragmentations of ^{19}F + ^{209}Bi in the LMT window around the most probable ⟨LMT⟩ = 78%. The detector angle Φ is measured with respect to the beam direction in the horizontal plane and Ψ the perpendicular angle, cf. Fig. 7. Also shown are the best fit results.

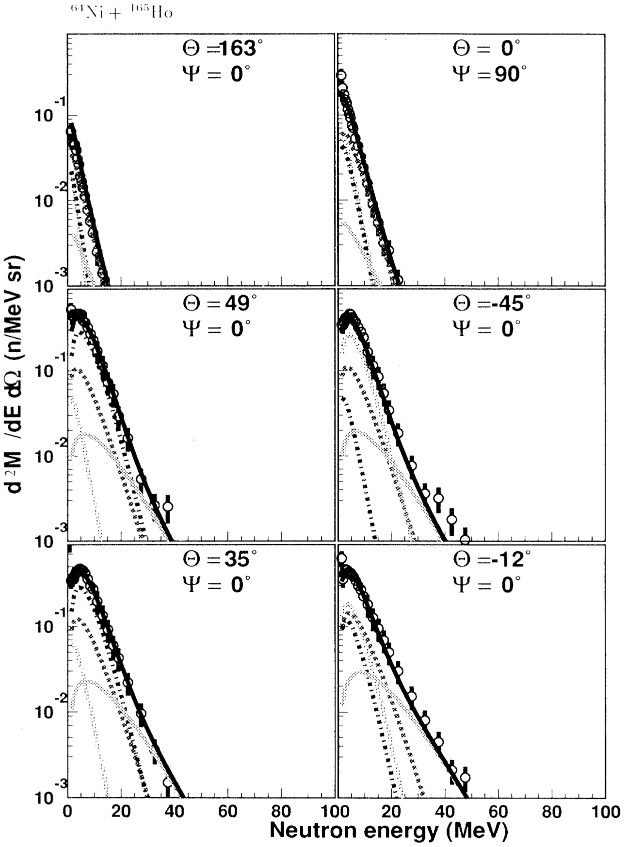

FIG. 5. Same as Fig. 4 for the reaction ^{64}Ni + ^{165}Ho. Only 6 out of 10 spectra are presented. The underlying fragmentation class is again the one for the most probable LMT, i.e., 98%, and symmetric fragmentations.

Sec. III C together with the fit results for the fragment class of the most probable LMT and symmetrical fragmentation. For the ^{19}F + ^{209}Bi reaction the PE and the CN sources are clearly separated, as one can see from the most forward spectra. On the other hand, the neutron yield is not visibly increased in the direction of the fragment motion. The postscission neutron multiplicity is small and the decomposition into prescission and postscission contributions is correspondingly uncertain. For the ^{64}Ni + ^{165}Ho reaction, the PE and CN sources are not as clearly separated, but the fragment sources are more pronounced. The small enhancement in forward directions corresponding to a low PE multiplicity makes the decomposition into PE and CN neutrons difficult, whereas the strong correlation with the fragment flight direction indicates a large postscission multiplicity.

TABLE III. Preequilibrium neutron multiplicities M_{PE}, temperatures T_{PE}, and source velocities ϵ obtained from the moving source fits. The parameter a_n describes the PE anisotropy out of the reaction plane (see Sec. IV A).

LMT	M_{PE}	T_{PE} (MeV)	ϵ (MeV/nucleon)	a_n
1(a)	6.3 ± 1.0	3.8 ± 0.4	3.9(57%) ± 0.9	—
1(b)	3.3 ± 0.6	4.0 ± 0.6	3.8(56%) ± 1.0	—
1(c)	1.1 ± 0.3	5.2 ± 1.3	3.7(55%) ± 1.9	—
1(d)	0.5 ± 0.4	6.0 ± 3.6	4.0(57%) ± 2.3	—
2(a)	3.4 ± 0.5	5.1 ± 0.6	6.2(49%) ± 1.5	1.4 ± 0.4
2(b)	3.4 ± 0.5	6.4 ± 0.8	4.6(42%) ± 1.3	1.1 ± 0.5
2(c)	3.0 ± 0.5	8.1 ± 1.3	4.6(42%) ± 1.6	1.1 ± 0.5
2(d)	1.8 ± 0.5	12.0 ± 3.2	4.4(41%) ± 2.3	1.4 ± 1.1

TABLE IV. Temperature and multiplicity parameters for the prescission and postscission neutron sources obtained from the moving source analysis for symmetrical fragmentations.

LMT	$M_{\rm pre}$ (MeV)	$T_{\rm pre}$	$M_{\rm post,1}$	$M_{\rm post,2}$ (MeV)	$T_{\rm post}$
1(a)	4.3 ± 1.0	3.2 ± 0.6	4.4 ± 0.7	4.5 ± 0.7	1.7 ± 0.2
1(b)	5.3 ± 1.0	3.4 ± 0.5	6.1 ± 0.9	6.4 ± 0.7	2.1 ± 0.2
1(c)	7.3 ± 1.1	3.5 ± 0.5	6.4 ± 0.9	6.4 ± 0.8	2.3 ± 0.2
1(d)	8.1 ± 1.1	3.7 ± 0.4	6.4 ± 0.9	6.2 ± 0.8	2.2 ± 0.2
2(a)	6.9 ± 0.5	2.5 ± 0.1	3.3 ± 0.5	3.2 ± 0.3	1.2 ± 0.1
2(b)	8.5 ± 0.6	3.0 ± 0.8	3.4 ± 0.8	3.5 ± 0.5	1.4 ± 0.2
2(c)	11.7 ± 0.7	3.2 ± 0.2	3.5 ± 0.8	3.7 ± 0.5	1.5 ± 0.2
2(d)	14.9 ± 0.9	3.4 ± 0.2	3.2 ± 0.9	3.7 ± 0.6	1.6 ± 0.3

The results from the moving source fits are listed separately for the PE source parameters in Table III and the equilibrium sources, i.e., the CN and the fragments, in Table IV.

C. Fission coincident α particles

In the experiment ^{19}F + ^{209}Bi, the spectroscopy of fission-coincident α particles was done using the supplementary twofold segmented surface barrier detector (SB$_\alpha$) positioned at $\Theta = 145°$ and 149° in the reaction plane. At these backward angles the α yield should be described by the compound nucleus source only, whereas the contributions of other sources should be negligible [2].

The double differential α distributions are shown in Fig. 6 for the three highest classes of excitation energies. Events with ranges corresponding to the detector thickness could not accurately be reconstructed in energy and were omitted in the spectra; this explains the gaps. For the lowest excitation energy class, only the average α multiplicity per fission event could be determined because of the low α yield.

The analysis of the high energy part of the α spectra above the Coulomb barrier V_C was performed with a modified [40] Watt distribution in order to guarantee a comparison with the corresponding results of the neutron analysis, in particular the CN temperature. Transformation to the laboratory frame yields the expression

$$\frac{d^2M_{\rm CN,\alpha}(E_\alpha,\Theta_\alpha)}{dE_\alpha d\Omega(\Theta_\alpha)} = \frac{M_{\rm CN,\alpha}}{2(\pi T_{\rm CN,\alpha})^{3/2}}\sqrt{E_\alpha}\exp\left[-\frac{E_\alpha + 4\epsilon_{\rm CN} - 4\sqrt{E_\alpha\epsilon_{\rm CN}}\cos\Theta_{\rm CN}}{T_{\rm CN,\alpha}}\right], \qquad (7)$$

which was applied to the high energy part. Here, the α energy in the laboratory system is reduced by the Coulomb energy, i.e.,

$$E_\alpha = E_{\rm kin} - V_C \qquad (8)$$

in order to take into account the Coulomb acceleration of the α particles in the field of the emitting nucleus. Hence, in a first approach the rising parts of the spectra below V_C were fitted by Gaussian distributions and the maxima identified with V_C, resulting in $V_C = 23 \pm 2$ MeV in the center-of-mass frame. This result is in good agreement with corresponding fusion barriers of the inverse process for $Z = 92$ [41]. There is no clear trend for V_C versus excitation energy as opposed to recently reported results by [42]. The data indicate neither a stronger deformation nor modified density distributions for the hotter nucleus.

In the next approach the high energy part is fitted using Eq. (7) with a fixed V_C in order to obtain the temperature parameter T_α. The multiplicities M_α imply an isotropic emission in the CN rest frame. The results of the fitting procedure are listed in Table V. A possible anisotropy in the CN α emission out of the reaction plane due to the angular momentum as reported by [2] would reduce M_α by approximately the same fraction for all fragmentation classes.

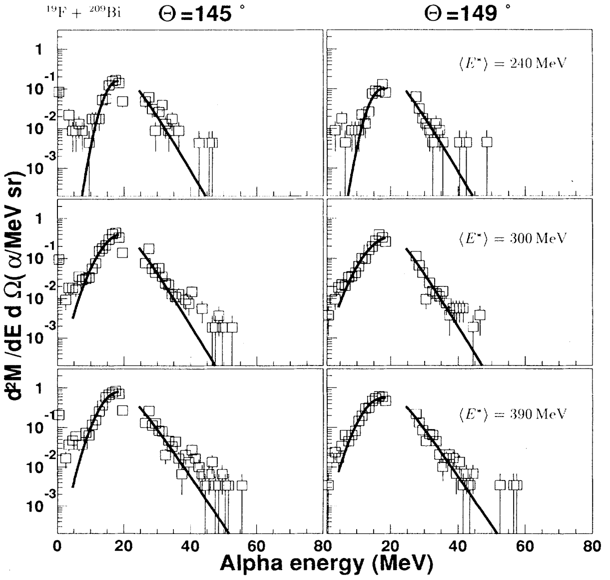

FIG. 6. Double differential α multiplicities (squares) for ^{19}F + ^{209}Bi and the three highest LMT windows (see Table II). The moving source fit includes only a CN source (solid line).

TABLE V. α multiplicities and temperatures for the CN source. $V_{C,\mathrm{cms}}$ the Coulomb barrier for α emission is obtained from the rising part of the spectra (see Fig. 6) and transformed into the cm system. The poor α statistics do not allow a fit of the spectral shape for the lowest LMT window.

LMT	M_α	T_{alpha} (MeV)	$V_{C,\mathrm{cms}}$ (MeV)
2(a)	0.01 ± 0.001	——	——
2(b)	0.3 ± 0.03	3.3 ± 0.3	22
2(c)	1.2 ± 0.1	3.6 ± 0.1	25
2(d)	3.2 ± 0.3	4.0 ± 0.1	25

IV. NEUTRON PREEQUILIBRIUM EMISSION

A. PE angular distribution

The angular distribution of the PE neutrons in the ^{19}F + ^{209}Bi experiment was measured with high accuracy by means of the position-sensitive plastic scintillator bars (SCB). In the reaction plane, which is defined by the flight directions of the fission fragments and is perpendicular to the spin of the CN (cf. Fig. 7), the PE angular distribution is well described; the PE source velocity ϵ_{PE} is the only free fit parameter. As expected [43], the best fit leads to ϵ_{PE} corresponding to half the projectile velocity with a tendency towards higher values for more peripheral collisions. However, the fit is unsatisfactory for the spectra accumulated out of the reaction plane. One observes a stronger reduction in the PE multiplicity with increasing angle with respect to the beam than in the reaction plane. This is shown qualitatively in Fig. 7 for two bins associated with the extreme positions $\Psi = 11^\circ$ and 43° covered by the SCB.

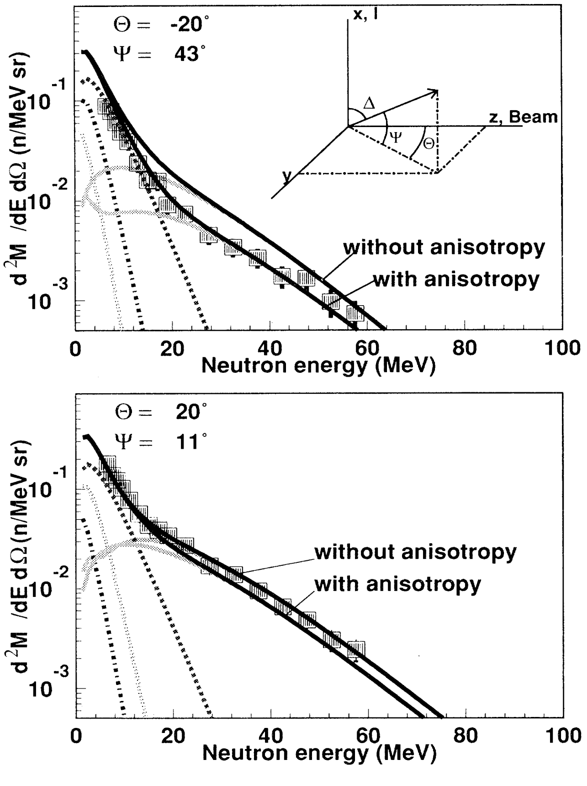

FIG. 7. Double differential neutron multiplicities measured with the position sensitive scintillator bars (squares) for the reaction ^{19}F + ^{209}Bi ($\langle$LMT$\rangle$ = 78% and symmetric fragmentation). Top: spectrum at the maximum out-of-plane position under $\Psi = 43^\circ$. Bottom: spectrum at the most downward position under $\Psi = 11^\circ$. Fits are performed with and without the assumption of an additional out of plane anisotropy (see text).

In order to describe this anisotropy quantitatively, one introduces a fit ansatz for the PE emission that factorizes the in-plane from the out-of-plane distribution [43], the latter being described by the polar angle Δ (cf. Fig. 7)

$$M_{\mathrm{PE}}(\Theta, \Delta) = M_{\mathrm{PE}}(\Theta) \exp\left[-a_n \cos^2(\Delta)\right]. \tag{9}$$

The anisotropy parameter a_n is a measure of the strength of the deviation from isotropy ($a_n \equiv 0$). Transformation into the laboratory frame leads to

$$\left(\frac{d^2 M_n}{dE\, d\Omega}\right)_{\mathrm{lab}} = \frac{M_n}{N(\pi T)^{3/2}} \sqrt{E_{\mathrm{lab}}} \times \exp\left(-\frac{E_{\mathrm{lab}} + \epsilon - 2\sqrt{E_{\mathrm{lab}}\epsilon}\cos(\Theta)}{T}\right) \times \exp\left(-\frac{a_n E_{\mathrm{lab}} \cos^2 \Delta}{E_{\mathrm{lab}} + \epsilon - 2\sqrt{E_{\mathrm{lab}}\epsilon}\cos(\Theta)}\right) \tag{10}$$

with the normalization constant

$$N = \int_0^\pi \sin\Delta \exp\left(-a_n \cos^2 \Delta\right) d\Delta \tag{11}$$

depending on a_n.

The best fit to the data in-plane as well as out-of-plane is included in Fig. 7, yielding a value $a_n = 1.1 \pm 0.5$. An anisotropy parameter $a_n = 1.1$ is synonymous with an overestimation of the PE multiplicity by 37% in a measurement restricted to the reaction plane. The parameter a_n shows no dependence on the underlying fragmentation class. Hence, the observed anisotropy cannot be attributed to an enhanced contribution of neutrons emitted by the projectile spectator.

The value for a_n is clearly smaller than the one reported by Zank *et al.* [43] of $a_n = 2.2 \pm 0.6$ for ^{12}C + ^{175}Lu ($E_P = 192$ MeV) determined by the same method. However, for the reaction ^{19}F + ^{209}Bi the absolute PE multiplicity $M_{\mathrm{PE}} = 3.0 \pm 0.5$ as well as its relative contribution to the total multiplicity of 14% is distinctly higher than for the reaction ^{12}C + ^{175}Lu ($M_{\mathrm{PE}} = 0.4 \pm 0.1$ or 5%, respectively). This makes the system ^{19}F + ^{209}Bi more suitable for analyzing the PE component. Tsang *et al.* reported a reduction of 50% for protons with kinetic energies above 30 MeV corresponding to an a_p of 0.7 [44]. However, this result is based on one out-of-plane measurement only.

The measured anisotropy exhibits the relation between incomplete fusion, PE emission and angular momentum reduction. As discussed in Sec. III A, the cross section for central collisions estimated with a sharp-cutoff approximation leads to partial waves up to $40\hbar$ above the critical angular momentum $l_{\rm crit}^{(B)} = 82\hbar$ of the Bass model for the reaction ^{19}F + ^{209}Bi . This demonstrates that the fused nucleus might reduce its angular momentum during the early stages of its evolution towards this stability limit. This can be done effectively by PE emission, but only if the emission occurs in the reaction plane perpendicular to the spin of the CN fissioning later on.

B. PE emission and dissipation

In this section the observed PE parameters, i.e., the multiplicities and most probable LMT values [whose uncertainties can be estimated from Figs. 2(c) and 2(d)] on the one hand and the temperature parameters on the other, will be compared to a Boltzmann master equation (BME) calculation with the code RELAX [8]. Here, the analysis is restricted to the fragmentation class centered on the most probable LMT.

The experimental results, including those for the ^{32}S + ^{197}Au system from [9], are listed in Table VI. One has to keep in mind that the PE multiplicities for the ^{64}Ni + ^{165}Ho as well as for the ^{32}S + ^{197}Au systems are only upper limits, due to the restriction to the reaction plane.

An essential parameter of the BME model is the initial number of excitons, n_0. In a first approach, n_0 was set to the number of projectile nucleons. The resulting PE multiplicities and most probable LMT values are in reasonable agreement with our data, cf. Table VI. The temperature parameters, however, tend to deviate in all three cases, though partly within the experimental uncertainties stated. Whereas the calculated temperature parameter exceeds the experimentally observed one for the reactions ^{19}F + ^{209}Bi and ^{32}S + ^{197}Au , the more symmetric entrance channel ^{64}Ni + ^{165}Ho with the heaviest projectile shows a trend in the opposite direction.

Therefore, a second approach was to modify accordingly the parameter n_0, which relates the excitation energy to the PE temperature via $E^* = (n_0 - 1)T_{\rm PE}$ [51]. The results of this approach are also listed in Table VI. These values n_0 lead by construction to the correct PE temperature parameters. In addition, they show the same trend to smaller n_0 for more symmetric entrance channels as reported by [45] for inclusive proton spectra and systems with comparable projectile energy. The same trend in n_0 was observed [19] for the reaction ^{20}Ne +^{165} Ho with $E_p = 402$ MeV (i.e., $E^* = 325$ MeV) yielding $M_{n,\rm PE} = 2.3$ and $T_{\rm PE} = 7.7$ MeV; this spectral data could be best reproduced with $n_0 = 24 - 28$, and with $n_0 = 23$ [8], respectively. However, this calculation fails to describe the PE multiplicities and therefore also the most probable LMT. In particular, the linear momentum loss, which was measured with an accuracy better than 2%, deviates by a factor of more than 2.

The description of the PE emission in the framework of the BME model thus deteriorates with increasing projectile mass number. This may be due to a longer injection time $\tau_{\rm inj}$ for reactions with heavier projectiles. In the BME model, projectile injection is treated with the fractional volume of the projectile, which passes through a plane in a single time increment at a constant velocity, namely the relative velocity in the center-of-mass system above the Coulomb barrier [8]. Due to the lower projectile velocity and the larger projectile volume, the injection of ^{64}Ni + ^{165}Ho should therefore take longer than for the systems ^{19}F + ^{209}Bi and ^{32}S + ^{197}Au. If there were now an additional delay for the formation, this would lead to higher calculated PE temperatures and smaller PE multiplicities. This is shown qualitatively in Fig. 8. Figure 8(a) shows the kinetic energy released in PE neutron emission as a function of time.

The injection is completed at $\tau_{\rm form} = 1.4 \times 10^{-22}$ s and 3.4×10^{-22} s for the ^{19}F and ^{64}Ni induced system, respectively. The definition of the preequilibrium time is more subjective. According to [8], the equilibration time $\tau_{\rm PE}$ is taken as the time the rate of neutron emission ceases to accelerate. For both systems $\tau_{\rm PE}$ is (6–8)$\times 10^{-22}$ s. Thus for ^{19}F + ^{209}Bi , $\tau_{\rm form}$ is considerably smaller than $\tau_{\rm PE}$ (cf. Fig. 8), and the BME model leads to a steeper temporal evolution of the PE multiplicity as well as PE temperature. This indicates that any additional delay in the injection time for the ^{64}Ni + ^{165}Ho system would lead to higher PE temperatures and smaller PE multiplicities at the end of the preequilibrium time, which shows only little variation with projectile target combination and relative projectile velocity [8].

Evidence for a delayed formation for the more symmetric entrance channel is indeed found in the enhancement of asymmetric mass splits for the ^{64}Ni induced reaction. Obviously, for the system ^{64}Ni + ^{165}Ho the kinetic energy of the entrance channel is dissipated before the composite system becomes spherical (if at all), i.e., the mass

TABLE VI. Comparison of experimental data with results of a BME calculation with different choices for n_0.

Reaction		$M_{n,\rm PE}$	LMT	$T_{\rm PE}$ (MeV)
^{64}Ni + ^{165}Ho	Experiment	1.1 ± 0.9	98%	5.2 ± 1.3
	BME $n_0 = 64$	1.4	96%	4.3
	BME $n_0 = 52$	2.7	93%	5.0
^{32}S + ^{197}Au	Experiment	4.1 ± 0.3	74%	8.0 ± 0.5
	BME $n_0 = 32$	4.6	79%	9.5
	BME $n_0 = 41$	3.1	87%	7.8
^{19}F + ^{209}Bi	Experiment	3.0 ± 0.5	78%	8.1 ± 1.3
	BME $n_0 = 19$	3.0	81%	10.0
	BME $n_0 = 24$	2.2	88%	8.3

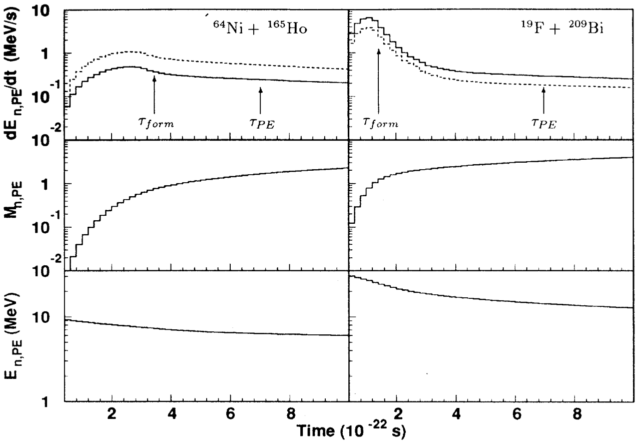

FIG. 8. Evolution of the kinetic energy $dE_{n,\mathrm{PE}}/dt$ removed by PE neutrons (top), PE neutron multiplicity $M_{n,\mathrm{PE}}$ (middle), and average kinetic energy emitted by PE neutrons $E_{n,\mathrm{PE}} = \frac{3}{2}T_{\mathrm{PE}}$ (bottom). The quantities are calculated with 2×10^{-23} s increments in the framework of the BME model for a $n_0 = A_p$ (solid lines). For $dE_{n,\mathrm{PE}}/dt$ a calculation with the modified n_0 is shown, too. The end of the formation phase τ_{form} as well as the end of the thermalization phase τ_{PE} are indicated by arrows.

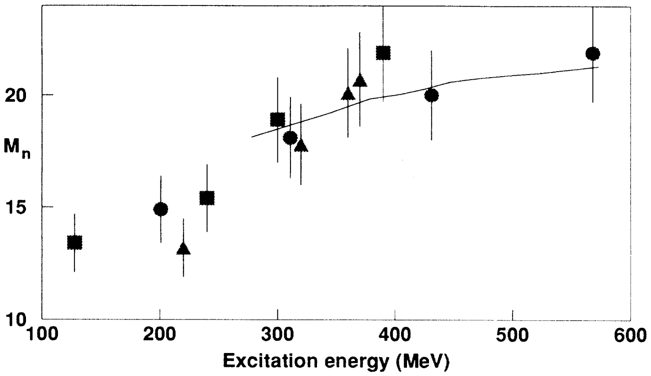

FIG. 9. Total neutron multiplicities M_n without contribution of PE neutrons vs excitation energy for ^{19}F + ^{209}Bi (squares), ^{32}S + ^{197}Au (dots) [9], and ^{64}Ni + ^{165}Ho (triangles). The solid line represents the results of an independent 4π neutron scintillator tank measurement [31] for ^{32}S + ^{197}Au with approximately half of the PE multiplicity contributing to M_n.

asymmetry degree of freedom is not equilibrated. On the other hand, the neutron source fit yields the same temperature parameters for the lighter as well as for the heavier fragment source; this demonstrates that the energy is fully equilibrated at the scission point.

V. EMISSION FROM THE EQUILIBRIUM SOURCES

A. Neutron multiplicities

From the observed most probable LMT values it follows that a large part of the initial excitation energy is already carried away during the preequilibrium phase, namely 4% and 23% for the ^{64}Ni- and ^{19}F-induced reactions and the most probable fragmentation classes, respectively. The subsequent evolution for the compound nuclei and the nascent fragments will be discussed in this section.

The discussion starts with the multiplicities of neutrons from the CN (M_{pre}) and the fragments (M_{post}), which were obtained for the different excitation energies of the underlying fragmentation classes.

The total multiplicities M_{tot} without PE contributions are plotted in Fig. 9 and show the same dependence on the excitation energy for both reactions. For each additional ΔE^* of 26 MeV, they increase by one neutron for excitation energies up to 400 MeV. However, a neutron typically carries away an excitation energy of approximately 10 MeV–13 MeV, indicating that only about half of the additional excitation energy is carried away by neutrons in this energy region.

The two reactions under study show distinct differences if M_{tot} is split into M_{pre} and M_{post} and considered in its dependence on E^* (Fig. 10). For the reaction ^{19}F + ^{209}Bi, M_{pre} increases with E^* in the same way as the total multiplicity, whereas the postscission multiplicity does not vary with E^*. The same trend was observed for the systems ^{32}S + ^{144,154}Sm, ^{197}S, and ^{232}Th [6,9]. Hence, independent of the underlying partial wave distribution for these systems, additional excitation energy is carried away before scission occurs, and the CN at the scission point is cold compared to the initial excitation energy. This familiar behavior is attributed to a slow fission process.

For the reaction ^{64}Ni + ^{165}Ho, the situation is completely different. Here both M_{pre} and M_{post} increase slightly with E^* and, more important, the major part of the total multiplicity stems from the fragments, i.e., the postscission sources. The latter indicates that the ^{64}Ni-induced reaction generates a clearly more excited system than ^{19}F + ^{209}Bi, and its quasifission process is relatively fast. The quantitative discussion of the time scales for both reactions is deferred to Sec.VI.

For energies above 400 MeV (here one has only measurements for the system ^{32}S + ^{197}Au with the neutron time-of-flight technique [9] as well as with the 4π-scintillator tank [31]), the total multiplicities level off. This trend is indicative of competition with charged particle evaporation, which increases with the excitation energy and will be discussed next.

B. Fragment and CN temperatures

The postscission multiplicities suggest that the composite nucleus from the ^{64}Ni + ^{165}Ho reaction is more excited at scission than the one from the ^{19}F induced reaction. This would be in line with the higher fragment temperatures T_{post} plotted versus E^* in Fig. 11 and shall be quantified now. For the fragmentation class around the most probable LMT value of 98% (78%) for the ^{64}Ni- (^{19}F-)induced reaction, the neutron source fit yields a fragment temperature of 2.3 ± 0.2 MeV (1.5 ±

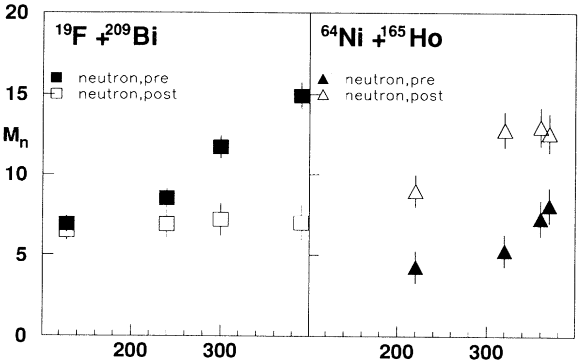

FIG. 10. Prescission and postscission neutron multiplicities (open symbols) for the reactions $^{19}\mathrm{F} + {}^{209}\mathrm{Bi}$ (left) and $^{64}\mathrm{Ni} + {}^{165}\mathrm{Ho}$ (right) vs initial excitation energy.

0.2 MeV). The excitation energy at the beginning of the fragment cascade can be estimated from these temperatures T_{post} as

$$E^*_{\mathrm{fragm}} = aT^2_{\mathrm{init}} = \frac{A_{\mathrm{fragm}}}{8}\left(\tfrac{12}{11}T_{\mathrm{post}}\right)^2 = \begin{cases} 32 \pm 8\,\mathrm{MeV} & \text{for} \quad {}^{19}\mathrm{F} + {}^{209}\mathrm{Bi}\,, \\ 83 \pm 13\,\mathrm{MeV} & \text{for} \quad {}^{64}\mathrm{Ni} + {}^{165}\mathrm{Ho}\,. \end{cases} \tag{12}$$

Here a value $A_{\mathrm{fragm}}/8\,\mathrm{MeV}^{-1}$ with the fragment mass number $A_{\mathrm{fragm}} \approx 100$ has been used for the level density parameter a. This choice of the level density is reliable for excitation energies below 100 MeV [46]. On the other hand, the fragment excitation energy carried away by neutrons is given by

$$E^*_{\mathrm{fragm}}(n) = M_{\mathrm{post}}\left(\tfrac{3}{2}T_{\mathrm{post}} + S_n\right) = \begin{cases} 38 \pm 5\,\mathrm{MeV} & \text{for} \quad {}^{19}\mathrm{F} + {}^{209}\mathrm{Bi}\,, \\ 76 \pm 10\,\mathrm{MeV} & \text{for} \quad {}^{64}\mathrm{Ni} + {}^{165}\mathrm{Ho}\,, \end{cases} \tag{13}$$

with a separation energy $S_n = 8.3\,\mathrm{MeV}$ of a fragment neutron. A comparison of Eq. (13) with Eq. (12) shows that neutron emission totally exhausts the accessible excitation energy.

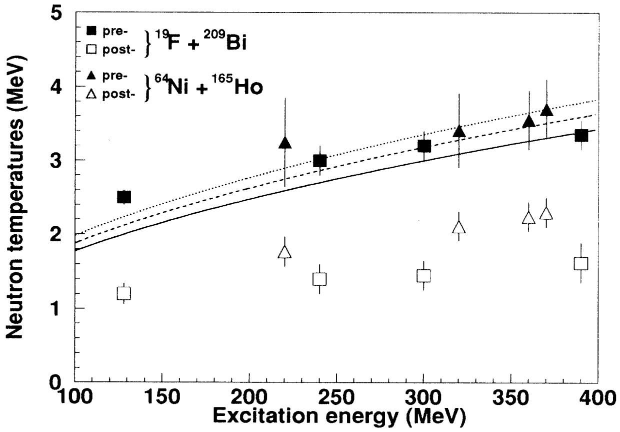

FIG. 11. Prescission and postscission neutron temperatures (open symbols) for $^{19}\mathrm{F} + {}^{209}\mathrm{Bi}$ (squares) and $^{64}\mathrm{Ni} + {}^{165}\mathrm{Ho}$ (triangles) vs initial excitation energy. The lines show the expected increase of the CN temperature $T(E^*_{\mathrm{CN}})$ for a constant level density parameter $A/10\,\mathrm{MeV}^{-1}$ (dotted), $A/9\,\mathrm{MeV}^{-1}$ (dashed), and $A/8\,\mathrm{MeV}^{-1}$ (solid).

Starting from the initial excitation energy of one fragment the excitation energy of the composite system at the scission point can be reconstructed as

$$E^*_{\mathrm{scission}} = 2E^*_{\mathrm{fragm}} + \langle\mathrm{TKE}\rangle - Q_{\mathrm{fiss}} = \begin{cases} 50\,\mathrm{MeV} & \text{for} \quad {}^{19}\mathrm{F} + {}^{209}\mathrm{Bi}\,, \\ 170\,\mathrm{MeV} & \text{for} \quad {}^{64}\mathrm{Ni} + {}^{165}\mathrm{Ho}\,. \end{cases} \tag{14}$$

Here, E^*_{fragm} is taken from Eq. (12), the measured average total kinetic energies $\langle\mathrm{TKE}\rangle$ are 165 MeV (156 MeV), and the fission Q values taken from [33] are 163 MeV (170 MeV) for the ^{64}Ni- (^{19}F-)induced reaction. Equation (14) confirms that the reaction with ^{64}Ni indeed results in a reaction system that is a factor of 3 more excited at scission than through the ^{19}F channel.

Figure 11 shows that the temperatures T_{pre} for neutron emission from the compound nucleus do not increase as steeply with increasing excitation energy as one would expect from $\frac{12}{11}\,T_{\mathrm{pre}} = \sqrt{E^*/a}$ with a constant level density parameter between $a = A_{\mathrm{CN}}/10$ and $A_{\mathrm{CN}}/8\,\mathrm{MeV}^{-1}$. This becomes more obvious if one compares the neutron emission temperatures in Fig. 12 with those for α emission from the reaction $^{19}\mathrm{F} + {}^{209}\mathrm{Bi}$. The α temperatures are higher in all cases. The difference is approximately described by the factor $\frac{12}{11}$, which is the relation between the apparent temperature over the whole deexcitation cascade and the initial temperature at the beginning of the cascade [47], if one kind of particles, here neutrons, covers the whole deexcitation cascade and the level density parameter is constant. It indicates that the neutron temperatures describe the average temperature, whereas the α temperatures can be identified with the initial temperatures. Hence, the α particles are emitted at the beginning of the cascade. At this time the excitation energy and the angular momentum are still high enough to favor, and the deformation is not too strong to hinder, the emission of α particles. Further-

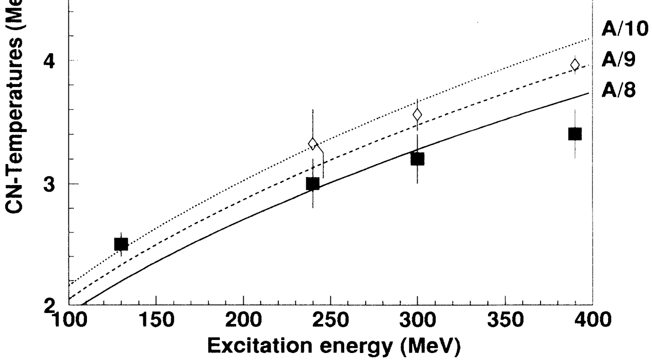

FIG. 12. Prescission α temperatures (diamonds) and neutron temperatures (squares) for the reaction $^{19}\mathrm{F} + {}^{209}\mathrm{Bi}$ vs initial E^*. The lines $T(E^*_{\mathrm{CN}})$ correspond to those in Fig. 11.

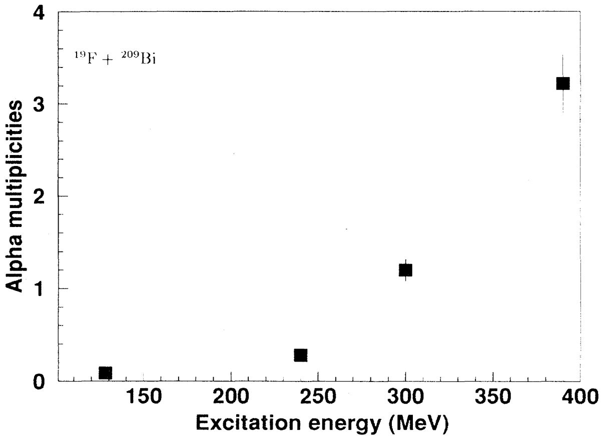

FIG. 13. Prescission α multiplicities per fission event vs initial E^*.

more, Fig. 12 demonstrates that α temperatures are in agreement with a constant level density parameter a between $A_{\rm CN}/10$ and $A_{\rm CN}/9$ MeV^{-1}. We will make use of this value for the statistical model calculation, which will be discussed in Sec. VI.

As already mentioned, the excitation cascade of the fragments is dominated by neutron emission. For the composite system with excitation energies between 200 MeV and 400 MeV, however, only less than half of the excitation energy is carried away by neutrons. For $E^* > 400$ MeV, the total neutron multiplicity even begins to saturate with increasing E^*. This trend reflects the increasingly dominant competition with charged particle evaporation. As an example we measured the α multiplicity for the system ^{19}F + ^{209}Bi. The dependence $M_\alpha(E^*)$ (Fig. 13) confirms our interpretation of the saturation of neutron multiplicity and of the neutron temperature. Below $E^* \approx 200$ MeV, there is no noticeable α particle evaporation. Above this energy, α emission sets in and rises quickly with an average increase of 46 MeV per additional α particle. One can assume a typical energy $\langle E_{\alpha,\rm kin}\rangle + \langle S_\alpha\rangle$ of 22 MeV carried away by one α particle. Hence, above $E^* = 200$ MeV about half of the excitation energy is carried away by α particles.

VI. FISSION TIME SCALES

A. The neutron clock

So far it has been emphasized that for the ^{19}F + ^{209}Bi reaction most of the initial excitation energy is carried away *before* scission, whereas for the ^{64}Ni + ^{165}Ho reaction a large amount of excitation energy is removed *after* scission. This exhibits distinctly a longer prescission lifetime for the ^{19}F -induced reaction than for the ^{64}Ni-induced one. The prescission lifetimes for the systems under study will now be discussed quantitatively with reference to the *neutron clock method* [1]. This method assumes that the statistical model, with appropriate parametrization, describes correctly the emission rates of light particles such as n, p, d, t, and α, but excludes the description of the competing fission channel, because it cannot take into account the time needed for the rearrangement of nuclear matter. For excitation energies above approximately 50 MeV, this delay time becomes longer than the entire statistical lifetime. The particle emission time τ is defined by the corresponding decay width Γ via $\tau = \hbar/\Gamma$ with $\Gamma(E^*, I)$, e.g., for neutrons given by

$$\Gamma_n(E^*, I) = \frac{(2s_n+1)}{2\pi\rho(E^*, I)} \times \sum_{I=0}^{\infty} \sum_{J=I-l}^{J=I+l} \int_0^{E^*-S_n} \rho(E^* - S_n - \epsilon_n, J) \times T_l(\epsilon_n)\, d\epsilon_n. \tag{15}$$

Here, s_n denotes the spin of the emitted particle, l its angular momentum, ϵ_n its kinetic energy, and S_n its separation energy. The transmission coefficients $T_l(\epsilon_n)$ are calculated from optical model potentials.

With Eq. (15) the fission lifetime is traced back to the ratio of the level densities $\rho(E^*, I)$ of the final nucleus and the decaying nucleus, depending on the excitation energy and spin of the nuclei. The level densities are not well known for high excitation energies, because the assumption of emission from an equilibrated system becomes questionable. For high excitation energies the emission time becomes shorter than typical relaxation times [48], which leads to uncertainties concerning the underlying level density parameter. Hence, the calculated absolute time scales are sensitive to the choice of the level density parameter. However, the relative time differences for the systems under study are not affected, as long as one takes the same level density parameter for all calculations. Here, a level density parameter $a = A/10$ MeV^{-1} was selected, first, to guarantee the compatibility of the results with the results for the ^{32}S + ^{197}Au reaction and second, to comply with the results for the α particle vs neutron emission temperatures (cf. Sec. V).

The calculation was performed for the fragmentation class around the most probable LMT value. As the initial spin we took the average of the partial wave distribution $\langle l\rangle = \frac{2}{3} l_{\rm crit}$, which is $55\hbar$ and $80\hbar$ for the ^{19}F- and ^{64}Ni-induced reaction, respectively. The initial excitation energy calculated from Eq. (5) was increased by 30 MeV to account for an average deformation energy. This value was taken from systematics reported by Hinde [4] for CN with masses of approximately 200 u.

In a first step, the deexcitation cascade is followed up to the last experimentally observed prescission neutron with the fission decay width $\Gamma_{\rm fiss}$ being switched off. From this point on, the full statistical decay width is switched on. One follows the whole deexcitation cascade for the remaining compound nucleus (which, because $\Gamma_n = \Gamma_{\rm fiss}$, may emit one more neutron before fission occurs), and then for those of the nascent fragments in order to complete the energy dissipation.

The energy balance resulting from this calculation is in good agreement with the experiment. Deviations are of the same order of magnitude as the estimated experimental errors of 10%. Hence, the time scale, which will be discussed now, seems to be reliable.

Figure 14 shows the fission time scales as a function of the prescission neutron multiplicity. The comparison with the experimentally observed prescission neutron multiplicity for symmetric fragmentations and the most probable LMT gives the fission time. For ^{64}Ni + ^{165}Ho it is 50×10^{-22} s, which is considerably shorter than for ^{19}F + ^{209}Bi with 160×10^{-22} s. The difference is even more pronounced if one takes into account the fragment acceleration phase. It comes about through neutrons, that are emitted after scission but before the fragment reaches 80% of its final velocity, and which are falsely identified as prescission neutrons [49]. For a typical fragment of mass 100 u and a TKE of 160 MeV, this acceleration phase lasts 20×10^{-22} s for both systems. Compared to the different neutron emission times of 10×10^{-22} s (40×10^{-22} s) for ^{64}Ni + ^{165}Ho (^{19}F + ^{209}Bi) at the scission point, this leads to an actual prescission neutron multiplicity, which is 2 (0.5) neutrons smaller than measured. If one reduces the prescission neutron multiplicity accordingly by these neutrons, one obtains a fission lifetime of $(30 \pm 5) \times 10^{-22}$ s and $(160 \pm 20) \times 10^{-22}$ s for the system ^{64}Ni + ^{165}Ho and ^{19}F + ^{209}Bi, respectively, from Fig. 14. The former is actually a quasifission lifetime, which results under a relaxation of the mass degree of freedom. The errors quoted were determined with an assumed uncertainty of one neutron in both cases. This is, however, a lower limit, because the neutron clock *ticks* with the time per neutron emission and cannot work more precisely. These uncertainties exclude systematic errors like ΔM_{pre} or the uncertainty of the underlying level density parameter. Nevertheless, in a first approximation these absolute uncertainties do not influence the comparison of fission times for different reactions.

In order to include the mass asymmetry degree of freedom in the considerations, the neutron clock method was extended to fragmentations with asymmetric mass splits. In Table VII the results of the different M_N windows for the ^{64}Ni- (^{19}F-)induced reaction are listed. The analysis was limited to those events with LMT values centered around the most probable one. During the fitting procedure, the preequilibrium source parameters were kept fixed at those values, which were determined for the corresponding symmetric fragmentation class.

In Fig. 15 the results for the prescission, postscission, and total neutron multiplicities are shown. The total multiplicities are in good agreement with JULIAN calculations. For asymmetric mass splits, the total neutron multiplicities decrease due to the smaller excitation energy available. Here, the higher Q value for fission overcompensates for the smaller TKE for asymmetric mass splits. However, the decrease in excitation energy will influence the particle emission only after scission. On the other hand, as one can see in Fig. 15, the prescission neutron multiplicity decreases, whereas the postscission multiplicity increases (for ^{19}F + ^{209}Bi) or remains constant, although the excitation energy after scission is lower. This is due to a shorter fission time for asymmetric fragmentations. Figure 16 shows a parabolic dependence of fission time vs mass asymmetry. For both reactions the fission time is a factor of 2 smaller for asymmetric mass splits ($0.2 < M_N < 0.4, 0.6 < M_N < 0.8$) than for symmetric mass splits ($0.4 < M_N < 0.6$) (see Table VII).

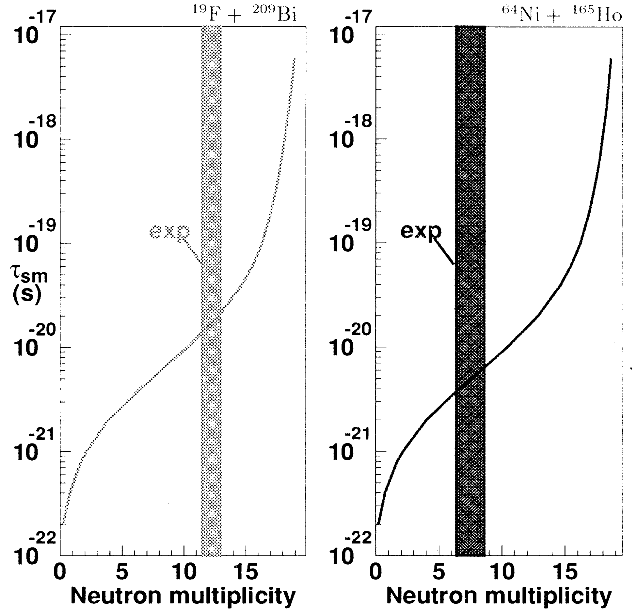

FIG. 14. Cumulative evaporation times (lines) calculated with a statistical model for a constant level density parameter $A/10\,\text{MeV}^{-1}$. The boxes give the experimental values of M_{pre} with their uncertainties.

TABLE VII. Comparison of symmetric and asymmetric fragmentation classes. The prescission and postscission multiplicities are those of the moving source analysis; the fission lifetimes τ_{sm} deduced from the neutron clock method are corrected for neutrons emitted during the acceleration phase.

Reaction	M_N window	$\langle M_N \rangle$	M_{pre}	$M_{\text{post},1}$	$M_{\text{post},2}$	τ_{sm} (10^{-22} s)
^{64}Ni + ^{165}Ho	10% – 40%	35%	6.7 ± 1.3	8.3 ± 1.5	3.7 ± 0.7	20 ± 10
	40% – 50%	46%	7.4 ± 1.4	6.8 ± 1.3	5.6 ± 0.8	30 ± 10
	44% – 56%	50%	7.3 ± 1.1	6.4 ± 0.9	6.4 ± 0.8	30 ± 10
	60% – 80%	67%	5.5 ± 1.3	4.1 ± 0.9	9.0 ± 1.2	10 ± 5
^{19}F + ^{209}Bi	20% – 40%	35%	9.0 ± 1.4	5.7 ± 1.5	2.5 ± 0.9	80 ± 20
	40% – 60%	52%	11.7 ± 0.7	3.7 ± 0.5	3.5 ± 0.8	160 ± 40
	60% – 80%	67%	9.2 ± 1.5	2.5 ± 0.7	5.6 ± 0.9	80 ± 20

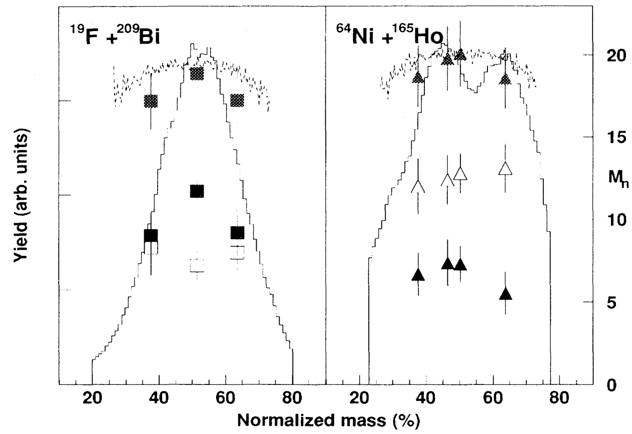

FIG. 15. Prescission (black symbols), postscission (open), and total multiplicities (gray) M vs mass split M_N for the reactions ^{19}F + ^{209}Bi (squares) and ^{64}Ni + ^{165}Ho (triangles). The dotted lines give the total neutron multiplicities from a JULIAN calculation that takes the M_N dependence of TKE and Q values into account. The total yield for fusion-fission events in the LMT class around the most probable LMT is also displayed.

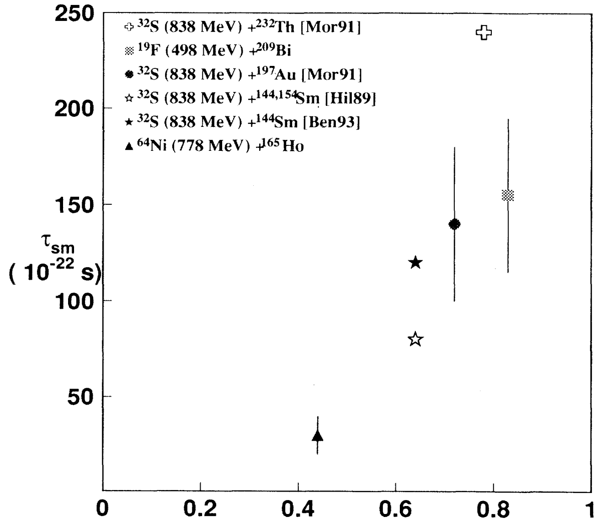

FIG. 17. Fission time vs mass asymmetry of the entrance channel for different reactions with some hundred MeV excitation energy and symmetric mass splits.

The same trend was already obtained for the systems ^{32}S + ^{144,154}Sm, ^{197}S, and ^{232}Th (E_p = 838 MeV) [6,9], which differ in fissility and contributions from deep inelastic reactions.

B. Interpretation of fission time scales

A comparison of fission time scales for symmetric mass splits as shown in Fig. 17 indicates a strong increase of fission times with *entrance channel* mass asymmetry. On the other hand, the fission time decreases with *exit channel* mass asymmetry. In this section it will be argued that both trends can be traced back to a common origin, namely the underlying rearrangement of nuclear matter.

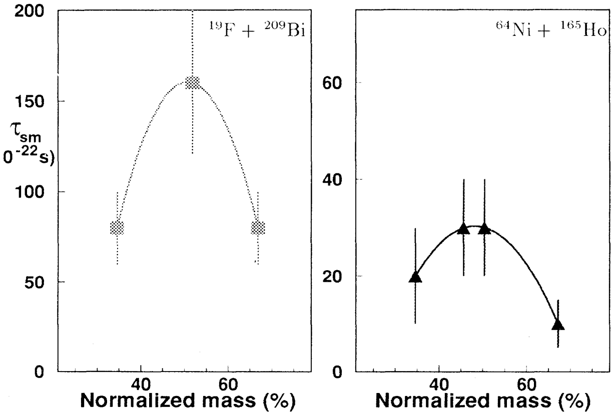

FIG. 16. Fission times τ_{sm} vs normalized mass M_N for ^{19}F + ^{209}Bi (squares, left) and ^{64}Ni + ^{165}Ho (triangles, right). The errors are estimated by varying the prescission multiplicities by one neutron. The parabolic lines guide the eye.

First, nondynamical causes are to be excluded. The restriction to symmetric fragmentations should exclude the strength of deep inelastic contributions as the cause of the different fission times.

Additionally, no clear dependence of τ_{sm} on the fissility or mass number $A_p + A_T$ is observed. This is because, due to the high temperatures and the high angular momenta for the reactions under comparison, one can assume that the fission barrier vanishes in almost all cases. Figure 18 shows the dependence of the fission barrier on angular momentum and temperature. For a neutron rich CN like ^{227}Pu with an angular momentum of $\approx 60\hbar$ and a typical temperature of 3.5 MeV, the fission barrier height is less than 1 MeV. Comparing this number with the available E^* of some hundred MeV, it is hard to believe that the fission barrier could hinder the evolution towards scission. Hence, the origin of the different time scales is supposed to be of dynamical nature.

The discussion starts with the development from the contact configuration towards the point of return, i.e., the point where the kinetic energy of the entrance channel is dissipated and the system enters the exit channel. The normalized mass distribution for the ^{64}Ni + ^{165}Ho reaction (Fig. 15) together with the observed opposite deviation of the PE parameters from BME calculations (Sec. IV B) lead us to assume a hindered formation of a spherical CN for the more mass-symmetric entrance channel. A delayed formation for more mass-symmetric entrance channels was already reported for the reactions ^{64}Ni + ^{100}Mo (E_p = 232 MeV) compared to ^{16}O + ^{148}Sm (E_p = 82 MeV) [16] and ^{64}Ni + ^{92}Zr (E_p = 233 MeV) [17]. However, for these reactions PE emission plays only a minor role and the delayed formation therefore comes about through the particle emis-

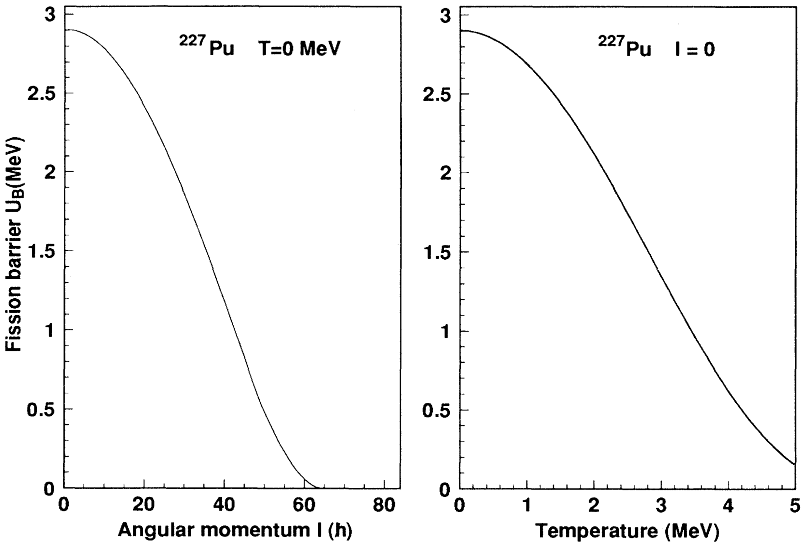

FIG. 18. Dependence of fission barriers B_f on angular momentum (from [37]) (left) and on temperature T (right) for the neutron deficient CN ^{227}Pu. Here, B_f was calculated with the weakest parametrization given in [50].

sion of the equilibrated CN. For the systems under study in this work, the projectile energy above 10 MeV per nucleon is considerably higher and the injection phase overlaps with the PE phase. Therefore, one can expect an experimental signature of a hindered injection mainly during the PE phase.

However, a longer injection time does not lead to a longer fission lifetime. That is because, due to the high projectile velocity, the injection time is small compared to the total fission lifetime in either case. On the contrary, the delayed injection is responsible for the fast fission process in the *exit channel.* This is shown schematically in Fig. 19. For the ^{19}F-induced reaction, the injection occurs quickly compared to the thermal equilibration time, and therefore the system in the exit channel develops from a spherical configuration towards scission. Due to the longer path from the spherical to the scission configuration, the corresponding time is long. For the ^{64}Ni-induced reaction, however, the kinetic energy of the entrance channel is dissipated before the spherical configuration is reached. The path from the deformed point of return to the scission point is short and so the time needed for scission is also short.

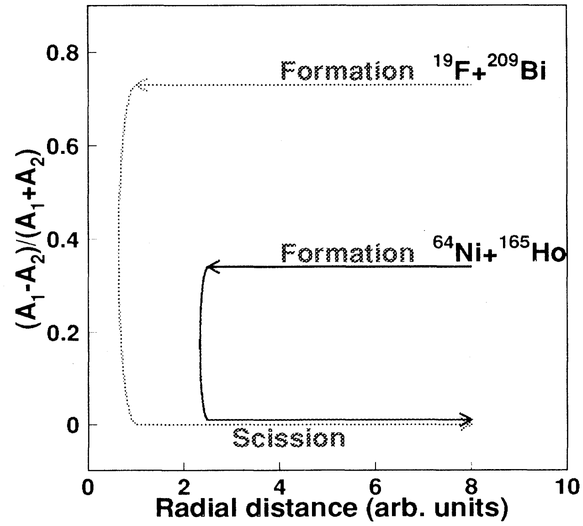

FIG. 19. Schematic trajectories in the radial distance vs mass asymmetry plane for entrance channels of different mass asymmetry (see text).

On the other hand, the development in the exit channel is influenced by the final mass asymmetry. It was shown that the asymmetric fragmentations are a factor of 2 faster than symmetric ones for *both* systems, although the amount of deep inelastic events is distinctly higher for the ^{64}Ni-induced reaction. This provides evidence for a consistent interpretation of the delayed injection and fission of the mass-symmetric initial and final configurations, respectively. One can assume that the development from the contact configuration towards the point of return, i.e., the injection process, and the development from the point of return towards the scission point, i.e., the fission process, are time inverse processes. Hence, both processes are determined by the need to rearrange nuclear matter. This necessity is higher for an evolution starting from a mass-symmetric initial configuration towards a more spherical configuration or, in time-reversed order, starting from a more spherical configuration towards a mass-symmetric final configuration. In both cases, the stronger the initial or final mass asymmetry (or, more precisely, the less nuclear matter has to be rearranged), the faster the evolution occurs. However, because the injection starts with the relative velocity in the center-of-mass frame above the Coloumb barrier, whereas the fission process starts at rest, the absolute time of the injection is small and does not contribute to the total reaction time.

To summarize, the fission time scales for highly excited nuclei are determined by an interplay of entrance and exit channel mass asymmetry.

VII. SUMMARY

We carried out the spectroscopy of neutrons by time of flight in coincidence with binary fission fragments for the reactions ^{64}Ni + ^{165}Ho with a projectile energy of 778 MeV or 12 MeV/nucleon, and for ^{19}F + ^{209}Bi with a projectile energy of 491 MeV or 26 MeV/nucleon. Both systems lead to composite nuclei with similar A and Z and with excitation energies E^* of up to 400 MeV. The experimental results for reactions with similar E^* and composite systems, in particular the reaction ^{32}S + ^{197}Au ($E_p = 838\,\text{MeV}$), were included in the data analysis.

The linear momentum transfer (LMT) was calculated from fragment velocity vectors and was converted into excitation energies in the massive transfer approach. The double differential neutron multiplicities have been unfolded for different fragmentation classes with respect to LMT or E^* and mass split M_N into contributions from four moving sources, namely a preequilibrium source, a prescission source, and two fragment sources with Maxwellian emission characteristics. Position-sensitive plastic scintillators allowed measurement of neutrons far out of the reaction plane.

The main results of the reactions under study are as follows.

(i) For the reaction ^{19}F + ^{209}Bi, the preequilibrium (PE) emission cannot be described adequately by an isotropic source. One observes a reduced emission out of the reaction plane, which is described by an anisotropy parameter of $a_n = 1.1 \pm 0.5$. This corresponds to a PE multiplicity 37% lower than deduced from a measurement made *only* in plane. This anisotropy is interpreted as outcome of PE emission contributing to the angular momentum depletion in order to decrease the angular momentum below the fusion stability limit.

(ii) The α emission from the equilibrium source is described by a temperature parameter, that is in agreement with calculated initial temperatures T_α, whereas the neutron emission temperatures are averages over the whole deexcitation cascade. This is due to the fact that α particles are emitted during the early stages of the deexcitation cascade. The increase of T_α with E^* indicates a constant level density parameter of $a = A_{\text{CN}}/10\,\text{MeV}^{-1}$. The saturation of the total neutron multiplicity with increasing E^* can be explained by an enhanced competition with α particle emission.

(iii) The reaction ^{64}Ni + ^{165}Ho favors an asymmetric mass split, whereas for the system ^{19}F + ^{209}Bi the normalized mass distribution is centered around $M_N = 0.5$. This observation, together with the opposite deviations of the PE source parameters from BME calculations for the ^{19}F- and the ^{64}Ni-induced reaction, respectively, speaks for a delayed injection for the more mass symmetric entrance channel.

(iv) The application of the neutron clock method to the prescission multiplicities leads to fission lifetimes of 30×10^{-22} s and 160×10^{-22} s for the reactions ^{64}Ni + ^{165}Ho and ^{19}F + ^{209}Bi, respectively, after correction for neutrons of the acceleration phase. These results refer to symmetric fragmentations and central collisions around the most probable LMT, which is 0.98 (0.78) for ^{64}Ni + ^{165}Ho (^{19}F + ^{209}Bi). A comparison of reactions with similar excitation energies indicates a trend to smaller fission times for more mass-symmetric entrance channels, which can neither be explained by different fissilities nor by different contributions from deep inelastic reactions.

(v) For all systems under comparison, asymmetrical fragmentations ($0.2 < M_N < 0.4$ and $0.6 < M_N < 0.8$) occur a factor of 2 faster than symmetric fragmentations. The height of the fission barrier and the contributions from deep inelastic events seem to have no visible impact on this ratio.

The observations (iii)–(v) are taken to be evidence for a dynamical effect: the evolution from a spherical configuration towards two fragments of similar mass, as well as the time-inverse process starting from a projectile plus a target of similar mass towards a spherical CN is hindered by the necessary rearrangement of nuclear matter. This applies only to a smaller extent to a mass-asymmetric configuration in the entrance *or* exit channel. Beyond this effect, a hindered injection can be explained by the faster development towards scission for the ^{64}Ni-induced reaction. Here, as in quasifission, a spherical CN is usually not reached and the development towards the scission point is accordingly faster.

ACKNOWLEDGMENTS

The authors thank the crew of the VICKSI accelerator for their continuous and successful efforts to provide an excellent beam. The help of Dr. M. Blann, who performed the BME calculations, is gratefully acknowledged. This work was financially supported by the Bundesministerium für Forschung und Technologie (Contracts No. 06 HH-175 and 06 HH-613) and by the Hahn-Meitner-Institut, Berlin (Contract No. F+E 151/531/8959).

---

[1] D. Hilscher and H. Rossner, Ann. Phys. (Paris) **17**, 471 (1992).
[2] F. Benrachi, D. Benchekroun, B. Chambon, B. Cheynis, D. Drain, C. Pastor, H. Rossner, D. Hilscher, B. Gebauer, D. Husson, A. Giorni, D. Heuer, A. Lleres, P. Stassi, and J. B. Viano, Phys. Rev. C **48**, 2340 (1993).
[3] D. J. Hinde, D. Hilscher, and H. Rossner, Nucl. Phys. **A502**, 497c (1989), and references therein.
[4] D. J. Hinde, Phys. Rev. C **45**, 1229 (1992).
[5] M. Thoenessen, D. R. Chakrabarty, M. G. Herman, R. Butch, and P. Paul, Phys. Rev. Lett. **59**, 2860 (1987).
[6] D. Hilscher, H. Rossner, B. Cramer, U. Jahnke, M. Lehmann, E. Schwinn, M. Wilpert, T. Wilpert, H. Frobeen, E. Mordhorst, and W. Scobel, Phys. Rev. Lett. **62**, 1099 (1989).
[7] M. Strecker, R. Wien, P. Plischke, and W. Scobel, Phys. Rev. C **41**, 2172 (1990).
[8] M. Blann, Phys. Rev. C **31**, 1245 (1985).
[9] E. Mordhorst, M. Strecker, H. Frobeen, M. Gasthuber, W. Scobel, B. Gebauer, D. Hilscher, M. Lehmann, H. Rossner, and Th. Wilpert, Phys. Rev. C **43**, 716 (1991).
[10] J. P. Lestone, J. R. Leigh, J. O. Newton, D. J. Hinde, J. X. Wei, Y. Chen, S. Elfström, and D. G. Popescu, Phys. Rev. Lett. **67**, 1078 (1991).

[11] J. P. Lestone, Phys. Rev. Lett. **70**, 2245 (1993).

[12] J. B. Natowitz, M. Gonin, M. Gui, K. Hagel, Y. Lou, D. Utley, and R. Wada, Phys. Lett. B **247**, 242 (1990).

[13] D. J. Hinde, J. R. Leigh, J. P. Lestone, J. O. Newton, S. Elfström, J. X. Wei, and Zielinska-Pfabe, Phys. Lett. B **258**, 35 (1991).

[14] J. Boger, J. M. Alexander, R. A. Lacey, and A. Narayanan, Phys. Rev. C **49**, 1587 (1994).

[15] A. Saxena, A. Chatterjee, R. K. Choundhury, S. S. Kapoor, and D. M. Nadkarni, Phys. Rev. C **49**, 933 (1994).

[16] M. Thoennessen, J. R. Beene, F. E. Bertrand, C. Baktash, M. L. Halbert, D. J. Horen, D. G. Sarantites, W. Spang, and D. W. Stracener, Phys. Rev. Lett. **70**, 4055 (1993).

[17] W. Kühn, P. Chowdhury, R. V. F. Janssens, T. L. Khoo, F. Haas, J. Kasagi, and R. M. Ronningen, Phys. Rev. Lett. **51**, 1858 (1983).

[18] P. Gippner, U. Brosa, H. Feldmeier, and R. Schmidt, Phys. Lett. B **252**, 198 (1990).

[19] E. Holub, D. Hilscher, G. Ingold, U. Jahnke, H. Orf, and H. Rossner, Phys. Rev. C **28**, 252 (1983).

[20] D. Hilscher, H. Rossner, A. Gamp, U. Jahnke, B. Cheynis, B. Chambon, D. Drain, C. Pastor, A. Giorni, C. Morand, A. Dauchy, P. Stassi, and G. Pettit, Phys. Rev. C **36**, 208 (1987).

[21] A. Chbihi, L. G. Sobotka, N. G. Nicolis, D. G. Sarantites, D. W. Stracener, and Z. Majka, Phys. Rev. C **43**, 666 (1991).

[22] G. Nebbia, K. Hagel, D. Fabris, A. Majaka, J. B. Natowitz, R. P. Schmitt, B. Sterling, G. Mouchaty, G. Berkowitz, K. Strozewski, G. Viesti, P. L. Gonthier, B. Wilkins, M. N. Namboodiri, and H. Ho, Phys. Lett. B **176**, 20 (1986).

[23] V. Viola, Nucl. Phys. **A502**, 531 (1989).

[24] K. Paasch, H. Krause, and W. Scobel, Nucl. Instrum. Methods Phys. Res. **221**, 558 (1984).

[25] E. Weissenberger, P. Geltenbort, A. Oed, F. Gönnenwein, and H. Faust, Nucl. Instrum. Methods Phys. Res. Sect. A **248**, 506 (1986).

[26] K. Knoche, Ph.D. thesis, Universität Hamburg, 1994, Hamburg.

[27] H. O. Neidel and H. Henschel, Nucl. Instrum. Methods **178**, 137 (1980).

[28] G. Dietze and H. Klein, Report No. PTB-ND-22, PTB Braunschweig, 1982.

[29] R. A. Cecil, B. D. Anderson, and R. Madey, Nucl. Instrum. Methods **161**, 439 (1979).

[30] T. N. Taddeucci, ATTENE-*Program for Neutron Flux Attenuation*, Los Alamos National Laboratory, 1987, private communication.

[31] K. Knoche, L. Sprute, W. Behrmann, E. Mordhorst, W. Scobel, M. Strecker, B. Cramer, B. Gebauer, D. Hilscher, U. Jahnke, and E. Schwinn, Z. Phys. A **342**, 319 (1992).

[32] L. Lüdemann, K. Knoche, W. Scobel, and K. Woller, Nucl. Instrum. Methods Phys. Res. Sect. A **334**, 495 (1993).

[33] A. H. Wapstra and K. Bos, At. Data Nucl. Data Tables **17**, 474 (1976).

[34] V. E. Viola, K. Kwiatkowski, and M. Walker, Phys. Rev. C **31**, 1550 (1985).

[35] R. Bock, Y. T. Chu, M. Dakowski, A. Gobbi, E. Grosse, A. Olmi, H. Sann, D. Schwalm, U. Lynen, W. Müller, S. Bjørnholm, H. Esbensen, W. Wölfli, and E. Morenzoni, Nucl. Phys. **A388**, 334 (1982).

[36] R. Bass, Nucl. Phys. **A213**, 45 (1974).

[37] A. J. Sierk, Phys. Rev. C **33**, 2039 (1986).

[38] G. Grégoire, C. Ngô, and B. Remaud, Nucl. Phys. **A383**, 392 (1982).

[39] C. Ngô, in *Proceedings of the Winter College on Fundamental Nuclear Physics*, Trieste, Italy, edited by K. Dietrich, M. Di Toro, and H. J. Mang (World Scientific, Singapore, 1984), p. 1231.

[40] T. K. Nayak, T. Murakami, W. G. Lynch, K. Swartz, D. J. Fields, C. K. Gelbke, Y. D. Kim, J. Pochodzalla, M. B. Tsang, H. M. Xu, and F. Zhu, Phys. Rev. C **45**, 132 (1992).

[41] L. C. Vaz and J. M. Alexander, Z. Phys. A **312**, 163 (1983).

[42] M. Gonin, L. Cooke, K. Hagel, Y. Lou, J. B. Natowitz, R. P. Schmitt, S. Shlomo, B. Srivastava, W. Turmel, H. Utsunomiya, R. Wada, G. Nardelli, G. Nebbia, G. Viesti, R. Zanon, B. Fornal, G. Prete, K. Niita, S. Hannuschke, P. Gonthier, and B. Wilkins, Phys. Rev. C **42**, 2125 (1990).

[43] W. P. Zank, D. Hilscher, G. Ingold, U. Jahnke, M. Lehmann, and H. Rossner, Phys. Rev. C **33**, 519 (1986).

[44] M. B. Tsang, C. B. Chitwood, D. J. Fields, C. K. Gelbke, D. R. Klesch, and W. G. Lynch, Phys. Rev. Lett. **52**, 1967 (1984).

[45] M. Korolija, N. Cindro, R. Ĉaplar, R. L. Auble, J. B. Ball, and R. L. Robinson, Nucl. Phys. **A516**, 133 (1990).

[46] W. Dilg, W. Schantl, H. Vonach, and M. Uhl, Nucl. Phys. **A217**, 269 (1973).

[47] K. J. Le Couteur and D. W. Lang, Nucl. Phys. **13**, 32 (1959).

[48] M. G. Mustafa, M. Blann, A. V. Ignatyuk, and S. M. Grimes, Phys. Rev. C **45**, 1078 (1992).

[49] D. J. Hinde, R. J. Charity, G. S. Foote, J. R. Leigh, J. O. Newton, S. Ogaza, and A. Chatterjee, Phys. Rev. Lett. **52**, 986 (1984).

[50] G. Sauer, H. Chandra, and U. Mosel, Nucl. Phys. **A264**, 221 (1976).

[51] R. Ĉaplar, M. Korolija, and N. Cindro, Nucl. Phys. **A495**, 185 (1989).